

# SANDIA REPORT

SAND2016-11650

Unlimited Release

Printed November 2016

# Using Muons to Image the Subsurface

Nedra D. Bonal<sup>1</sup>, Avery T. Cashion IV<sup>1</sup>, Grzegorz Cieslewski<sup>1</sup>, Daniel J. Dorsey<sup>1</sup>, Wendi Dreesen<sup>3</sup>, Adam Foris<sup>1</sup>, J. Andrew Green<sup>2</sup>, Timothy J. Miller<sup>1</sup>, Leiph A. Preston<sup>1</sup>, Barry L. Roberts<sup>1</sup>, David Schwellenbach<sup>2</sup>, and Jiann-Cherng Su<sup>1</sup>

<sup>1</sup>Sandia National Laboratories, <sup>2</sup>National Security Technologies, <sup>3</sup>Formerly NSTec, currently Los Alamos National Laboratory

Prepared by  
Sandia National Laboratories  
Albuquerque, New Mexico 87185 and Livermore, California 94550

Sandia National Laboratories is a multi-mission laboratory managed and operated by Sandia Corporation, a wholly owned subsidiary of Lockheed Martin Corporation, for the U.S. Department of Energy's National Nuclear Security Administration under contract DE-AC04-94AL85000.

Approved for public release; further dissemination unlimited.



Sandia National Laboratories

Issued by Sandia National Laboratories, operated for the United States Department of Energy by Sandia Corporation.

**NOTICE:** This report was prepared as an account of work sponsored by an agency of the United States Government. Neither the United States Government, nor any agency thereof, nor any of their employees, nor any of their contractors, subcontractors, or their employees, make any warranty, express or implied, or assume any legal liability or responsibility for the accuracy, completeness, or usefulness of any information, apparatus, product, or process disclosed, or represent that its use would not infringe privately owned rights. Reference herein to any specific commercial product, process, or service by trade name, trademark, manufacturer, or otherwise, does not necessarily constitute or imply its endorsement, recommendation, or favoring by the United States Government, any agency thereof, or any of their contractors or subcontractors. The views and opinions expressed herein do not necessarily state or reflect those of the United States Government, any agency thereof, or any of their contractors.

Printed in the United States of America. This report has been reproduced directly from the best available copy.

Available to DOE and DOE contractors from

U.S. Department of Energy  
Office of Scientific and Technical Information  
P.O. Box 62  
Oak Ridge, TN 37831

Telephone: (865) 576-8401  
Facsimile: (865) 576-5728  
E-Mail: [reports@osti.gov](mailto:reports@osti.gov)  
Online ordering: <http://www.osti.gov/scitech>

Available to the public from

U.S. Department of Commerce  
National Technical Information Service  
5301 Shawnee Rd  
Alexandria, VA 22312

Telephone: (800) 553-6847  
Facsimile: (703) 605-6900  
E-Mail: [orders@ntis.gov](mailto:orders@ntis.gov)  
Online order: <http://www.ntis.gov/search>



# Using Muons to Image the Subsurface

Nedra D. Bonal<sup>1</sup>, Avery T. Cashion IV<sup>1</sup>, Grzegorz Cieslewski<sup>1</sup>, Daniel J. Dorsey<sup>1</sup>, Wendi Dreesen<sup>3</sup>, Adam Foris<sup>1</sup>, J. Andrew Green<sup>2</sup>, Timothy J. Miller<sup>1</sup>, Leigh A. Preston<sup>1</sup>, Barry L. Roberts<sup>1</sup>, David Schwellenbach<sup>2</sup>, and Jiann-Cherng Su<sup>1</sup>

Sandia National Laboratories  
P.O. Box 5800  
Albuquerque, New Mexico 87185

## Abstract

Muons are subatomic particles that can penetrate the earth's crust several kilometers and may be useful for subsurface characterization. The absorption rate of muons depends on the density of the materials through which they pass. Muons are more sensitive to density variation than other phenomena, including gravity, making them beneficial for subsurface investigation.

Measurements of muon flux rate at differing directions provide density variations of the materials between the muon source (cosmic rays and neutrino interactions) and the detector, much like a CAT scan. Currently, muon tomography can resolve features to the sub-meter scale. This work consists of three parts to address the use of muons for subsurface characterization: 1) assess the use of muon scattering for estimating density differences of common rock types, 2) using muon flux to detect a void in rock, 3) measure muon direction by designing a new detector. Results from this project lay the groundwork for future directions in this field. Low-density objects can be detected by muons even when enclosed in high-density material like lead and even small changes in density (e.g. changes due to fracturing of material) can be detected. Rock density has a linear relationship with muon scattering density per rock volume when this ratio is greater than 0.10. Limitations on using muon scattering to assess density changes among common rock types have been identified. However, other analysis methods may show improved results for these relatively low density materials. Simulations show that muons can be used to image void space (e.g. tunnels) within rock but experimental results have been ambiguous. Improvements are suggested to improve imaging voids such as tunnels through rocks. Finally, a

muon detector has been designed and tested to measure muon direction, which will improve signal to noise ratio and help address fundamental questions about the source of upgoing muons.

## **ACKNOWLEDGMENTS**

Special thanks to Sammy Bolin, Dennis King, George Slad, and Elton Wright for their help moving NSTec's muon detector for measurements in the tunnel; Tony Dismore for assistance with tunnel logistics; David Bonal for data acquisition code used with Sandia's muon detector; Tracy Woolever for business support; Duane Smalley for muon simulations using GEANT code; David Schodt for image processing assistance; and Samantha Rogers for research assistance.

## CONTENTS

1. Introduction.....	10
1.1. Muon Detectors.....	11
1.2. Modes of Acquisition.....	11
1.3. Examples of Muon Imaging.....	13
2. Using muon scattering to estimate density differences .....	17
2.1. Introduction.....	17
2.2. Muon Measurements.....	17
2.3. Muon tomography of rock samples .....	19
2.4. Data Processing Methods.....	20
2.5. Results.....	21
2.5.1. Synthetic comparison using MCNP6 .....	24
2.5.2. Simulation Results.....	25
2.6. Conclusions.....	28
2.7. Acknowledgements.....	29
2.8. References.....	29
3. Using muon flux to detect a void in rock .....	30
4. Measuring muon direction .....	34
4.1. Abstract.....	34
4.2. Introduction.....	34
4.3. Materials .....	36
4.3.1. Mechanical Description and Frame Assembly .....	36
4.3.2. Electronics & Instrumentation.....	38
4.4. Single-Panel Interaction Position Determination.....	39
4.4.1. Triangulation by Timing .....	39
4.4.2. Position calculation by Magnitude .....	42
4.3. Multiple Panel Considerations .....	46
4.3.1. Directional Determination.....	46
4.3.2. Trajectory Tracking .....	47
4.4. Discussion .....	49
4.5. References.....	51
5. Conclusions .....	53
4. References .....	54
Appendix A: Sandia Muon Detector Frame Structural Analysis .....	55
Distribution .....	63

## FIGURES

Figure 1. Description of the three main research areas pursued..... 10

Figure 2. Drift tube detector: series of drift tubes in X and Y orientations. The expanded tube show electrons drifting toward the wire after the gas in the tube is ionized by a passing muon.	11
Figure 3. Tomographic imaging mode.....	12
Figure 4. Telescopic imaging mode.....	13
Figure 5. A book (low-Z) and a sphere of tungsten (high-Z) inside a lead box (top) with the corresponding muon image in 2D (bottom).....	14
Figure 6. Simulation results of muon flux after passing through a cube of rock (e.g. silica) with an air-filled tunnel.....	15
Figure 7. Photo (left) of mountain being imaged (right) from horizontally traveling muons in telescopic mode. The lighter area in the top portion of the figure on the right represent the mountain in the photo on the left. The lighter area in the bottom portion of the figure on the right is due to “noise” from muons detected from the opposite direction.....	16
Figure 8. Muon detector used for geological sample measurement. ....	18
Figure 9. Schematic showing muon tracking through the drift tube assembly.....	18
Figure 10. Muon detector operating configured tomographic mode .....	19
Figure 11. Point of Closest Approach (POCA) ray tracing reconstruction .....	20
Figure 12. Segmented scatter angle, DOCA and POCA values .....	21
Figure 13. Sample Density Relative to Muon Reconstruction Results.....	23
Figure 14. Comparison of Sample Density Relative to Muon Reconstruction Results.....	23
Figure 15. MCNP muon source model distribution (red dots and solid red line) overlayed on Figure 3 from Reyna (2008). .....	24
Figure 16. MCNP muon source model distribution (solid lines) overlayed on Figure 2 from Reyna (2008). Note that the MUTRON measurements cited at $89^\circ$ were collected from $86^\circ$ to $90^\circ$ (Matsuno et al., 1984). .....	25
Figure 17. Simulation of muon tomography scan of granite, concrete, and anhydrite samples. Voxels where scatter density per muon track length density for scatters greater than 0.5 degrees and $0.012 \text{ cm/cm}^3$ of track length density are shown.....	26
Figure 18. Simulated muon tomography scan of salt, fractured salt, and sandstone samples. Voxels where scatter density per muon track length density for scatters greater than 0.5 degrees and $0.012 \text{ cm/cm}^3$ of track length density are shown.....	27
Figure 19. Simulated muon tomography scan of limestone, marble, and pyrite samples. Voxels where scatter density per muon track length density for scatters greater than 0.5 degrees and $0.012 \text{ cm/cm}^3$ of track length density are shown. ....	28
Figure 20. Schematic of muon detector pointing at ventilation shaft from inside a tunnel. The gray area represents the granite rock with sloping elevation. The blue triangle represents the acceptance angle of the detector and the red line represents a vector from the center of the detector. Drawing not to scale. ....	31
Figure 21. Muon attenuation surface by angle relative to the detector for data set 4) horizontally (zenith angle = $58^\circ$ ) oriented inside the tunnel (target measurements). Figure 21 is oriented relative to Figure 20. ....	32
Figure 22. Muon attenuation surface by angle relative to the detector for data set 3) vertically oriented inside the tunnel. Figure 22 is oriented relative to Figure 20. ....	33
Figure 1: Exploded view of scintillator panel assembly (Left) and configurable frame (Right). 37	
Figure 2: Block schematic of instrumentation system and model of detector frame.....	39

Figure 4: (A) PVT scintillator panel with 3 PMTs attached at the corners. BNC cable intersection point is shown. (B) Pulses received on the 3 channels recorded. Small differences in arrival time can be seen. (C) Actual BNC cable intersection point compared to point computed from time differences. (D) Superimposed actual vs computed plot over scintillator panel. ....	42
Figure 5: Original industrial aluminum foil wrapping beneath the outer black plastic layer (Left) and Mylar wrapping installed with calibration hole grid sheet (Right). ....	43
Figure 6: Hole-grid calibration sheet installed on the PVT panel. The holes are covered with individual tabs of black electrical tape. The flashing LED is mounted in the rubber puck shown. ....	44
Figure 7: Results of machine learning algorithm trained on calibration data, tested on separate data. Four configurations of PMTs are shown: With only 2 PMTs (Top Left), with 4 PMTs and low gain (Top Right), with 3 PMTs and high gain (Bottom Left), and with 4 PMTs and high gain (Bottom Right). ....	45
Figure 8: Simulated random muon tracks (Left) and muon tracks computed from real data (Right). The model generated from the calibration dataset from the center panel was applied to all three scintillator panels. ....	48
Figure 1: Solidworks simulation of shaft with 3,000 [lbf] of sinusoidally distributed bearing load across collar cross section and elastically supported by bearing. ....	55
Figure 2: Solidworks simulation at 600 [lbf] total loading across (3) $\frac{1}{4}$ "-20 screws fastening the shaft collar to the indexing plate. ....	56
Figure 3: Solidworks simulation at 2100 [lbf] total loading across (6) grade 8, $\frac{1}{4}$ "-20 cap screws and zero frame stiffness. ....	57
Figure 4: Solidworks simulation at 2100 [lbf] total loading across (6) grade 8, $\frac{1}{4}$ "-20 cap screws and infinite frame stiffness.....	58
Figure 5: Solidworks simulation at 400 [lbf] lateral loading and 650 [lbf] vertical loading on columns.....	59
Figure 6: Tip-over load of upper frame oriented at $45^\circ$ .....	60
Figure 7: Solidworks simulation for 1.5x1.5" extrusion frame in a horizontal orientation with 1200 [lbf] of loading applied at outlying nodes.....	61
Figure 8: Solidworks simulation of 2000 [lbf] combined vertical force and inward rotating moment of 2700 [lbf-in] acting on each column beam.....	62

## TABLES

Table 1. Tabulated Muon Reconstruction Results .....	22
Table 2. Muon Reconstruction Results .....	22
Table 3. Geological sample summary for measurements and simulations .....	25
Table 1. Tabulated machine learning performance data comparing results from using 3 PMTs against results from using 4 PMTs at the same gain setting. ....	46
Table 2. Tabulated data of direction of movement of muons through the detector in horizontal east-west orientation. ....	47

## **NOMENCLATURE**

DOE	Department of Energy
SNL	Sandia National Laboratories
NSTec	National Security Technologies

## 1. INTRODUCTION

Locating and characterizing subsurface structures such as tunnels and underground facilities remains a difficult problem. Muons are subatomic particles produced in the upper atmosphere, which penetrate the earth's crust up to few kilometers. Their absorption rate depends on the density of the materials including fluids through which they pass. Measurements of muon flux rate at differing directions provide density variations of the materials between the sky and detector from those directions, similar to a CAT scan. Therefore, the use of muons for subsurface investigation seems promising. This work consists of three parts as illustrated in Figure 1 to address the use of muons for subsurface investigation: 1) assess the use of muon scattering for estimating density differences of common rock types that are relatively low density materials (e.g.  $2.0 - 3.0 \text{ g/cm}^3$ ), 2) detect a void in a large volume of rock using muon flux, 3) measure muon direction by designing a new detector.

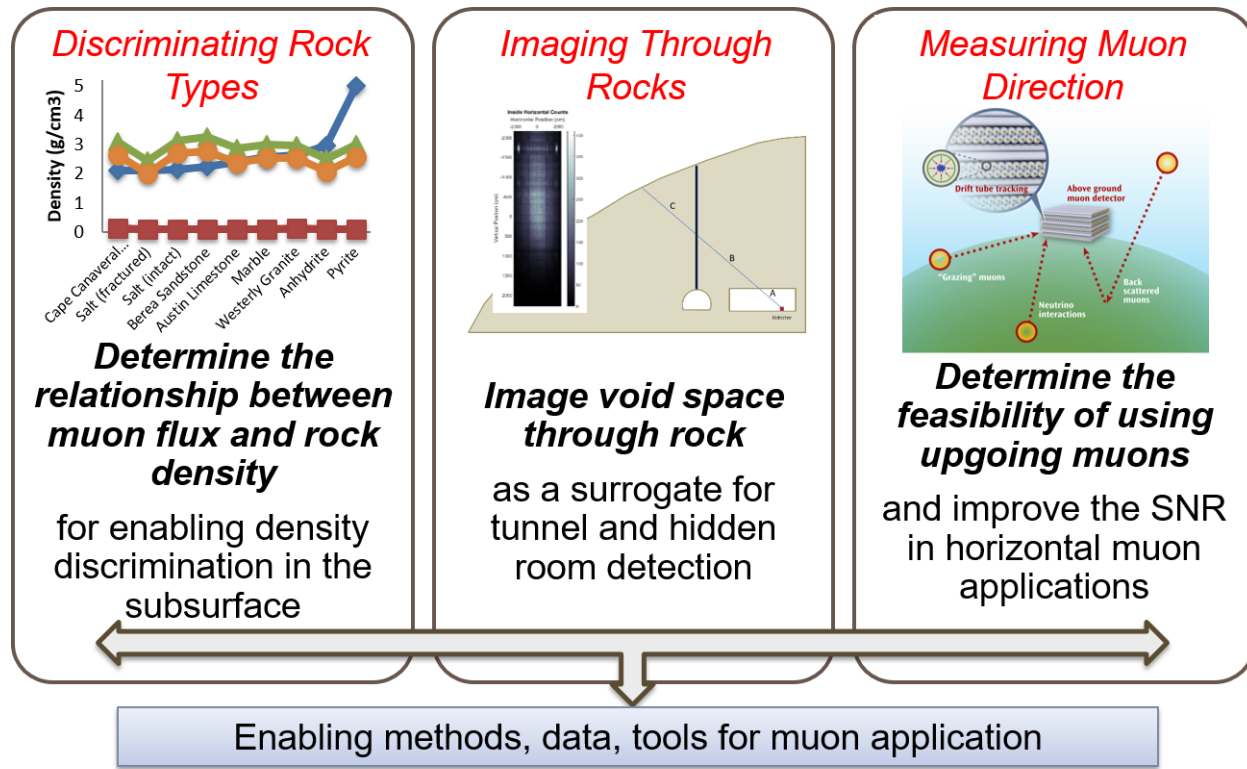


**Figure 1. Description of the three main research areas pursued.**

Alvarez et al. (1970) used muons to search for hidden chambers within the Egyptian pyramids. The results of Alvarez's work proved that the Pyramid of Khafre (the second pyramid) does not have any hidden chambers like those in the Pyramid of Khufu (the first pyramid). Nagamine et al. (1995) pioneered the technique of using muons to investigate volcanoes. Interest in using muons has expanded in recent years (Borozdin et al. 2003, Jourde et al., 2013, Lespare et al., 2010, Tanaka et al., 2003).

## 1.1. Muon Detectors

There are several types of instruments that can detect muons. The ones most commonly used for tracking muons include scintillation counters and gas wire detectors such as drift tubes and cathode strip chambers. When muons and other charged particles hit scintillating materials, photons are emitted through ionization. A photomultiplier is used to amplify the current to a measurable signal. Scintillators are typically used for counting/detecting muons. In gas wire detectors, electrons are knocked off the gas atoms when other charged particles pass through the gas. These electrons then drift toward the positively charged wire in the detector where gas amplification occurs creating a detectable signal. The distance away from the wire that the muon hit the gas can be determined by the time taken for the electrons to drift through the gas to the wire as shown in Figure 2 for the gas wire or drift tube example. A series of drift tubes are needed to increase the resolution of the muon hit location and track its path. Drift tubes are aligned in parallel and stacked in X and Y directions. The intersection between the X and Y tubes hit by a muon helps constrain the hit location. Multiple X and Y layers of tubes provide greater resolution and help eliminate charged particles other than muons. Drift tubes and scintillation counters are commonly used in accelerators for particle physics applications.

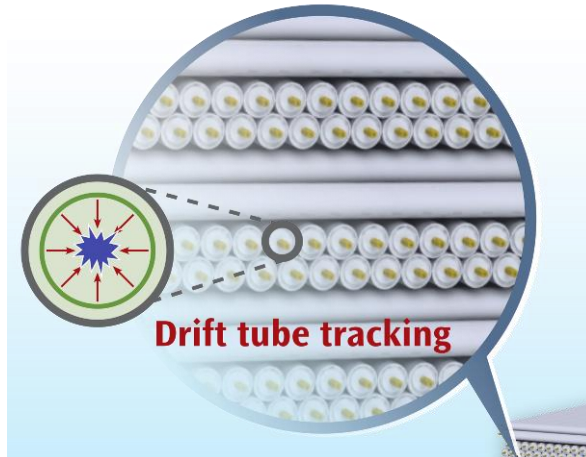


**Figure 2. Dirft tube detector: series of drift tubes in X and Y orientations. The expanded tube show electrons drifting toward the wire after the gas in the tube is ionized by a passing muon. The muon would have hit this tube tangent to the green circle.**

## 1.2. Modes of Acquisition

Two modes of data collection are discussed: the tomographic and telescopic. Additional methods including stopped tracks are often utilized but not addressed here. The tomographic mode uses two sets of muon detectors (Figure 3) to image objects between the two. Two detectors enables tracking of individual muons in and out of the column between them. The tomographic mode of imaging with muons relies on Coulomb scattering of the muons. The scattering angle of the muon is governed by density of the material the muon passed through (Figure 3). This angle can

be calculated using the two detectors for each muon and the material between the detectors can then be inferred. Additionally, the location and size of the material can be mapped in three-dimensions (example in Figure 5). A drawback to the tomographic mode is that access to two sides of the object is required, which may not be practical for many applications and ideally the objects need to be small enough to fit between the two detectors.

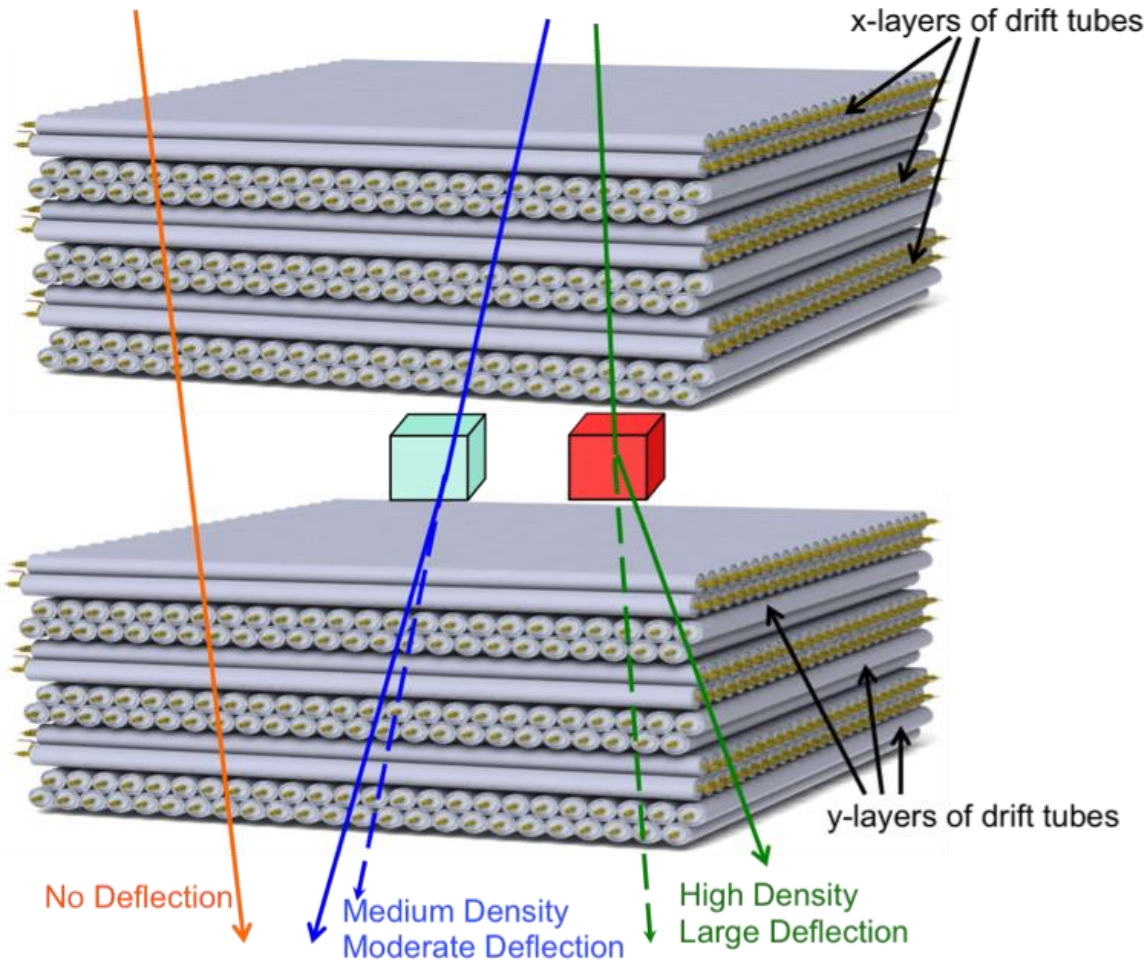


**Figure 3. Tomographic imaging mode.**

Telescopic mode requires only one detector, so access to only one side of the object is needed (Figure 4). This is sometimes referred to as transmission muon radiography and can produce 2D images of objects, similar to x-ray and gamma ray radiography. Also, very large objects like volcanoes can be imaged using this mode. However, lower resolution images are produced because the scattering angle of the muon through material cannot be measured. Additionally, acquisition times are typically longer since less information (no scattering angles) is obtained. The telescopic mode relies on attenuation of the number of muon (flux) passing through the materials because the incoming cosmic ray muon flux is fairly constant. More muons are attenuated in higher density materials so the flux is lower compared to lower density materials like air for example (Figure 4). Telescopic mode is often used to detect muons that are traveling nearly horizontally, like those needed to image a mountain.

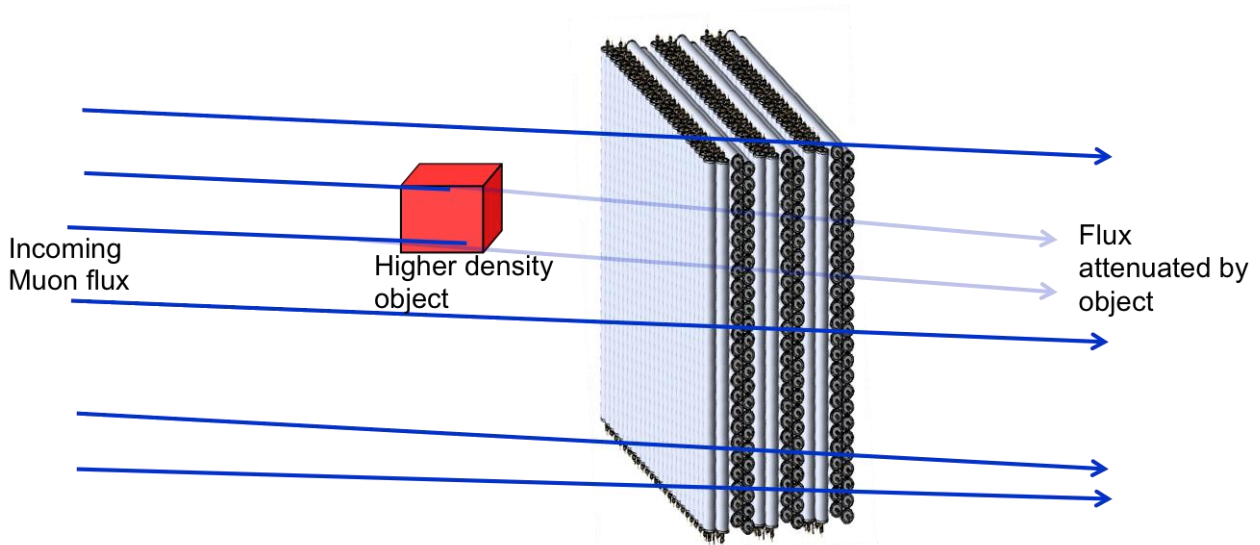


**Figure 4. Telescopic imaging mode**

### 1.3. Examples of Muon Imaging

Our current muon work includes density assessment and measuring muon direction. Improving our understanding in these areas will enhance muon images and increase the application space for muon imaging.

Muon fluxes are sensitive to densities. Therefore, muon data can be used to determine relative density differences of objects. Much work has been done using muons to detect high-density materials (Borozdin et al., 2003) but not low-density materials. We conducted a muon tomography experiment to detect of low-density material. A book (low density) and a sphere of tungsten (high density) were placed inside a lead box as shown in Figure 5 on the left. Muon data were collected over 1440 minutes (24 hours) using the tomographic mode. A 3D image of the lead box and contents was constructed from the muon hits and scattering angles. A horizontal slice of the 3D image is shown in Figure 5 on the right. Darker blues and reds in the reconstructed image represent higher density. The outline of the low-density book is also distinguished in the image. Though improvements can be made to further enhance the image in Figure 5, such as increasing acquisition time, this experiment demonstrates the feasibility of muon tomography for detection of low-density materials inside high-density material (e.g. the lead box).

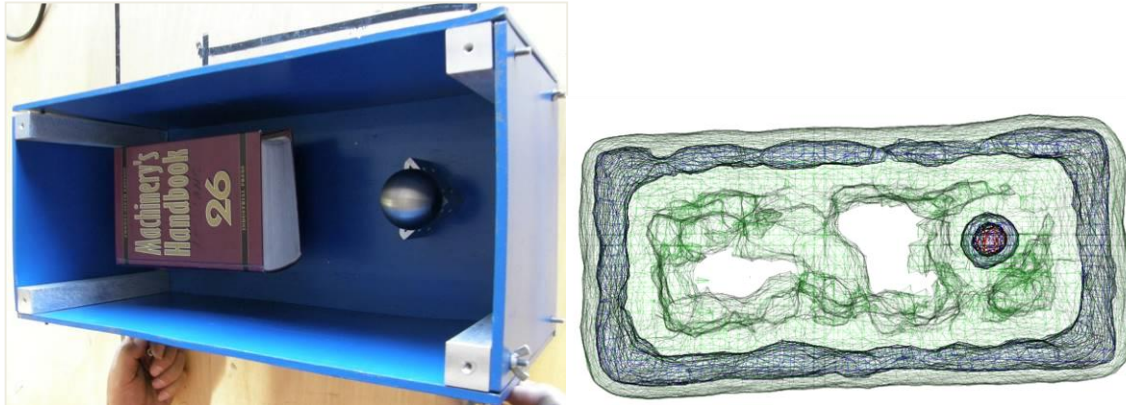


**Figure 5. A book (low-Z) and a sphere of tungsten (high-Z) inside a lead box (top) with the corresponding muon image in 2D (bottom).**

We also conducted a simulation of muon flux through rock with an air-filled void to demonstrate how muons can be used to map density changes using the telescopic mode. Figure 6 illustrates the layout of this simulation and the resulting muon image. A cube of silica representing standard rock with a density of  $2.65 \text{ g/cm}^3$  with an air-filled cylindrical hole in the center is hit with high-energy muons on one side and detected on the opposite side of the cube. The resulting muon image shows higher flux of muons around the cube (red), a moderate flux in the center where the void is located (green), and the lowest flux through the solid cube where there is no void (blue). This result is similar in concept to theoretical studies by Malmqvist et al. (1979). The Malmqvist et al. (1979) study found that density anomalies could be found using muon measurements, which would be applicable for prospecting specifically for massive sulfide and iron explorations.

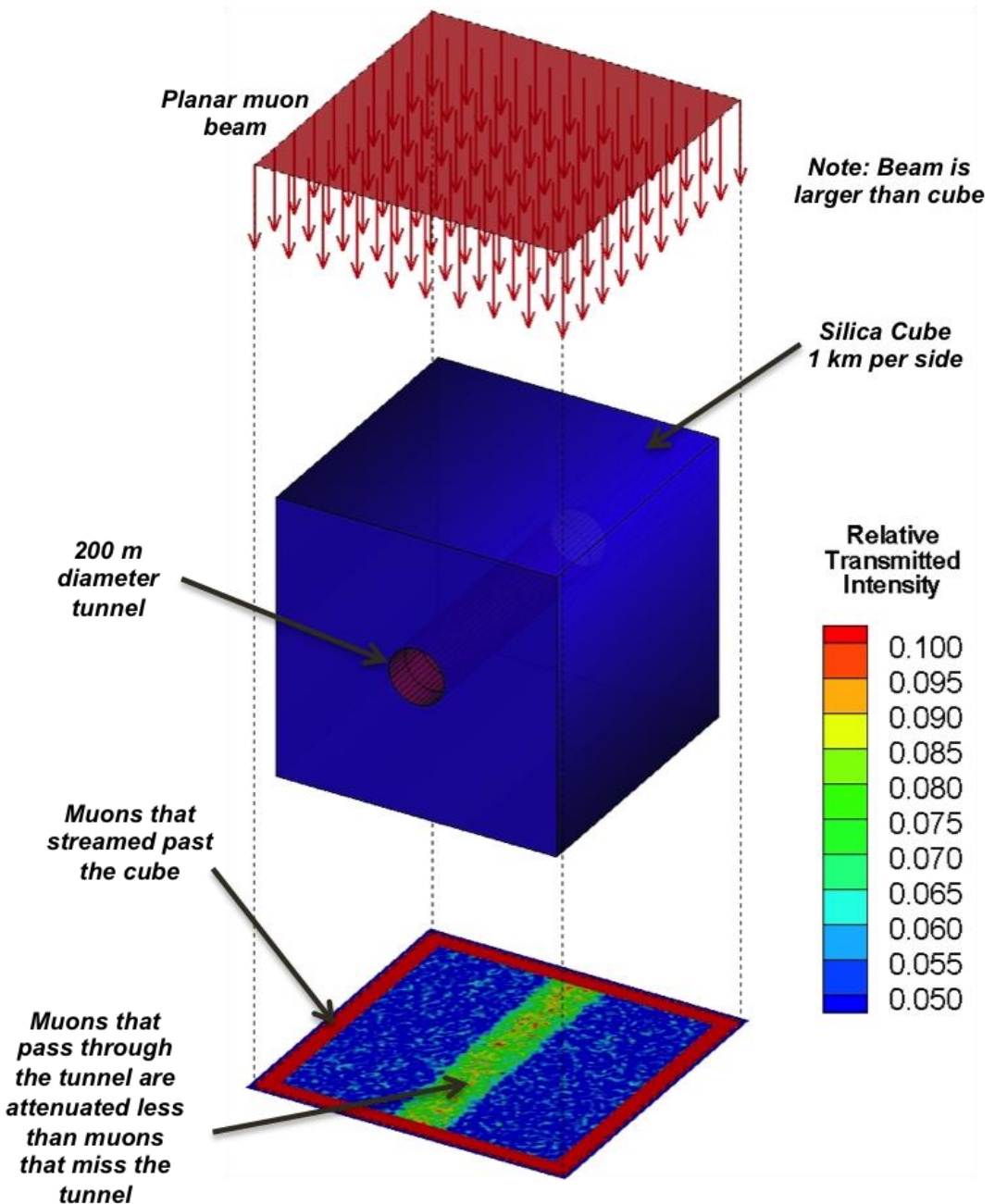


**Figure 6. Simulation results of muon flux after passing through a cube of rock (e.g. silica) with an air-filled tunnel.**

Determining the direction a muon is traveling is important for some applications. Detectors record muons coming from the direction of the object of interest and from the opposite direction. This is usually not a problem when imaging objects using vertically traveling muons because muons traveling upward are insignificant compared to the large flux of downward traveling muons. Muon flux decreases with zenith angle by approximately  $\cos^2$ . This means that the greatest flux is from muons traveling vertically downward from a zenith angle of  $0^\circ$  and the flux

is significantly lower from muons traveling horizontally with a zenith angle of  $90^\circ$ . Imaging targets like mountains requires use of muons traveling nearly horizontally at high zenith angles. For this case, the flux of muons from the desired direction is on the order of the flux from the opposite direction, resulting in a significant amount of “noise” (Figure 7). Determining the directionality each muon is traveling will eliminate this source of noise. Longer acquisition times will also increase the resolution of the image.



**Figure 7. Photo (left) of mountain being imaged (right) from horizontally traveling muons in telescopic mode. The lighter area in the top portion of the figure on the right represent the mountain in the photo on the left. The lighter area in the bottom portion of the figure on the right is due to “noise” from muons detected from the opposite direction.**

## **2. USING MUON SCATTERING TO ESTIMATE DENSITY DIFFERENCES**

### **2.1. Introduction**

Muons are subatomic particles sensitive to density that may be used to predict the material the muon passed through. Most muons are produced from cosmic ray collisions in the upper atmosphere and reach the earth at a rate or flux of about  $10^4$  particles/m<sup>2</sup>/min (at sea level for muons traveling from zenith angles near 90°). Muons are naturally occurring elementary particles similar to electrons except with about 200 times greater mass. Muons are highly penetrating and can travel several hundred meters through the earth due to their high energies. When muons pass through materials, they undergo multiple Coulomb scattering. The amount of scattering depends on material density, atomic number (Z), and the muon path length through the material. The highly penetrating nature and dependence on density makes muons useful for subsurface assessment and characterization. For example,

This work aims to assess the capability of muon scattering to discriminate variations in densities of common rock types that are relatively low density materials (e.g. 2.0 – 3.0 g/cm<sup>3</sup>). Ultimately, the goal is to estimate the rock density and thus infer rock type from the muon data to characterize the subsurface. To do this, muon tomography scans were completed for various rock types and the angular scattering was measured for each muon.

### **2.2. Muon Measurements**

Tomographic images of rock samples were used to measure muon scattering and relate it to sample density. The muon detector used for this study is shown in Figure 8 with three samples of geologic rocks in the center on the imaging target platform. This is a drift tube detector, which uses aluminum tubes filled with a gas mixture and a wire through the long axis of the tube. Electrons are knocked off the gas atoms when charged particles pass through the gas. These electrons then drift toward the positively charged wire in the detector where gas amplification occurs creating a detectable signal. The distance away from the wire that the muon hit the gas can be determined by the time taken for the electrons to drift through the gas to the wire as shown in Figure 9 for the gas wire or drift tube example. A series of drift tubes are needed to increase the resolution of the muon hit location and track its path. Drift tubes are aligned in parallel and stacked in X and Y directions. The intersection between the X and Y tubes hit by a muon helps constrain the hit location. Multiple X and Y layers of tubes provide greater resolution and help eliminate charged particles other than muons.



**Figure 8. Muon detector used for geological sample measurement.**

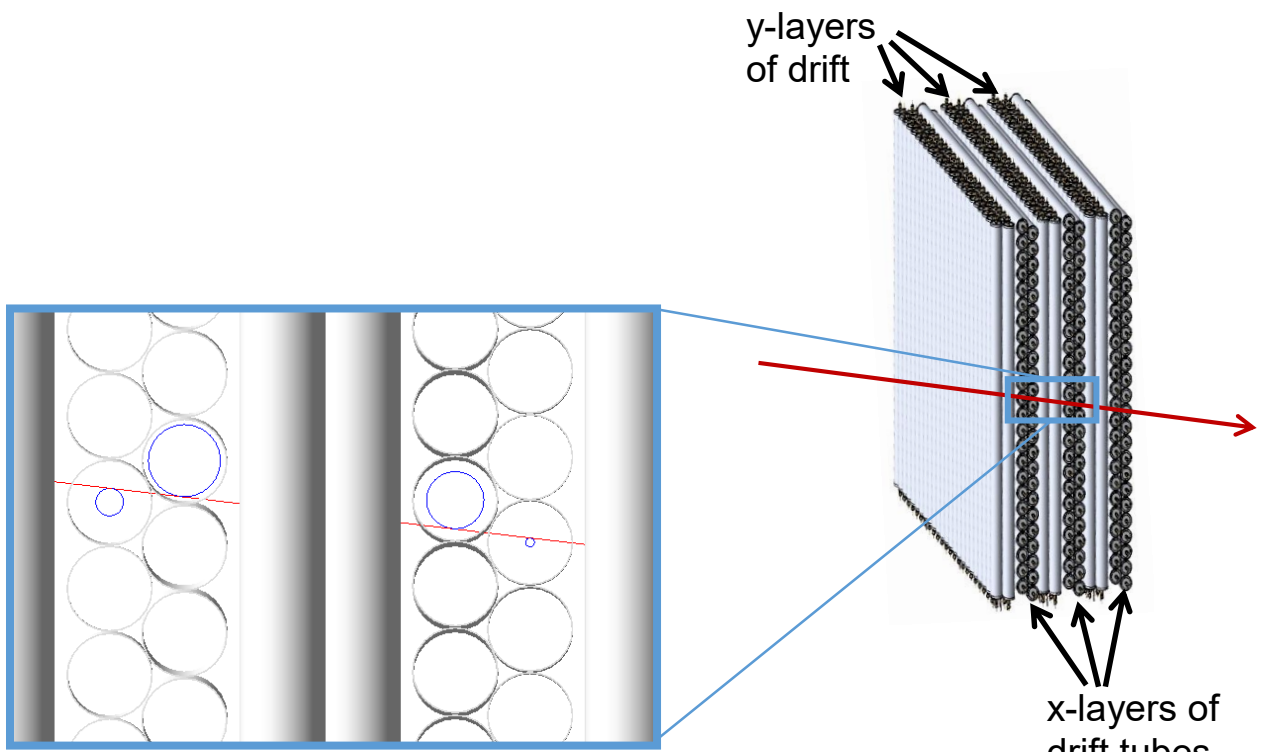


**Figure 9. Schematic showing muon tracking through the drift tube assembly.**

The detector operates by recording coincident counts through the upper and lower drift tube sections of the detector to determine a muon's flight path and estimate energy. Deviations between upper and lower trajectories are used to infer scatter events in post processing.

### 2.3. Muon tomography of rock samples

Tomographic images of rock samples were used to measure muon scattering and relate it to sample density. Three experiments were in tomographic mode as shown in Figure 10. The top and bottom muon flux sensors measures the time, position and direction of each muon that passes through them. Then, the sequential muon strikes from each sensor occurring within a maximum time threshold are correlated by the detector's software to estimate the muon's incoming and outgoing position and vector plus an estimation of its momentum. Estimated muon strike frequency for the detector is 100 strikes per second for these experiments. The datasets for each experiment are acquired for 22 to 23 hours.

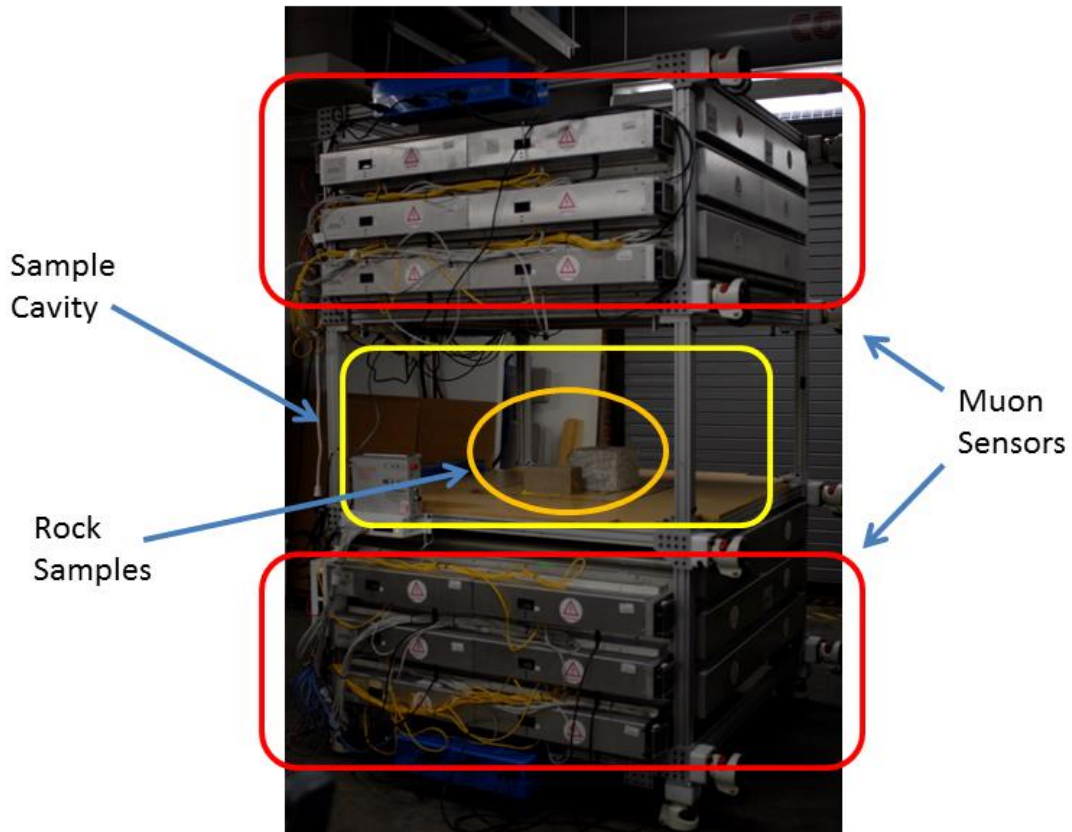


**Figure 10. Muon detector operating configured tomographic mode**

When a muon passes through an object, its path is scattered based on the thickness and density of the object. For these experiments, rock samples are placed between the sensors while each sensor measures the incoming and outgoing muon flux. The premise is to estimate the relative rock

densities based on the accumulated location and scatter angle of each muon from the aggregated data produced by the detector using simple radiography techniques.

## 2.4. Data Processing Methods

Two radiography methods were implemented to process and visualize the data acquired by the muon detector. The first, modeled after the Point of Closest Approach (POCA) reconstruction algorithm documented by Shultz (2003), showed promising results in its ability to observe the locations and sizes each sample as shown in Figure 11. The ray tracing technique evaluates each voxel in the measurement volume with the mean square scattering per unit length of the muons for that voxel Schultz (2003).

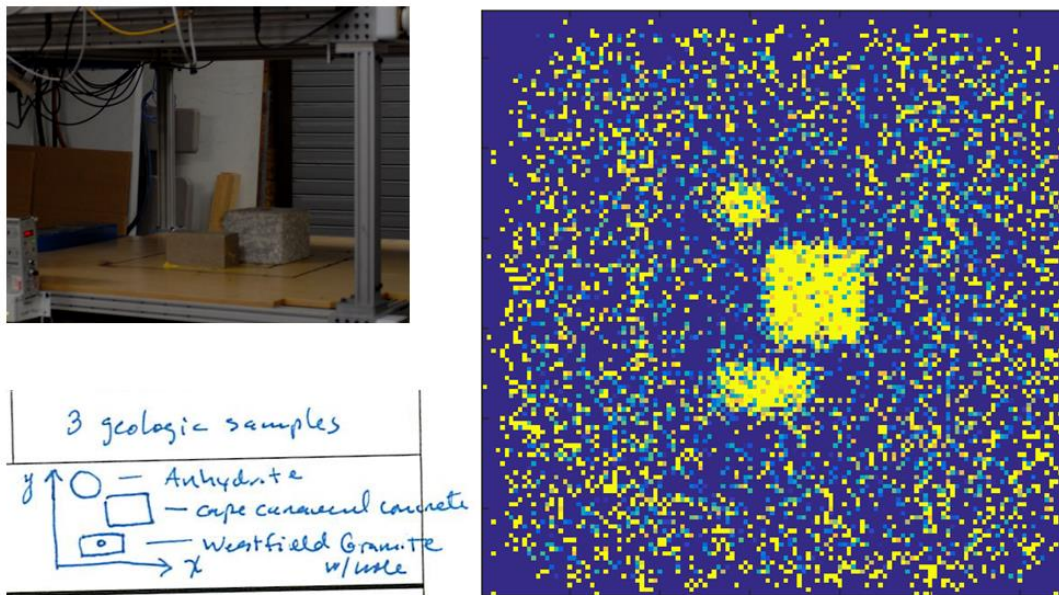


**Figure 11. Point of Closest Approach (POCA) ray tracing reconstruction**

The second technique is a POCA technique differing from the first in that it accumulates number and angle for each scatter location within the measurement volume of the detector based on the muon's incoming and outgoing vectors. The 3D lines coincident with the incoming and outgoing vectors measured by the detector for each muon are evaluated to determine the point where the distance between them is a minimum (i.e., the POCA or the intersection). In addition, the angle between the lines as well as the minimum distance between them is evaluated and accumulated at the coinciding POCA voxel location. The distance between the 3D lines is commonly referred to as the Distance of Closest Approach (DOCA) and is theorized that denser materials not only cause larger scatter angles but also exhibit large distances between the incoming and outgoing muon paths at POCA locations. After the resulting POCA, DOCA and scatter angle results are accumulated for each voxel, the resulting volume is visualized using ParaView (2016) volume rendering capability and the volumes for each sample are manually segmented from the overall volume. The segmented volumes can then be evaluated to compare the relative scatter angle,

POCA and DOCA values for each rock sample as shown in Figure 12. The values from each sample are then tabulated and evaluated to calculate density.

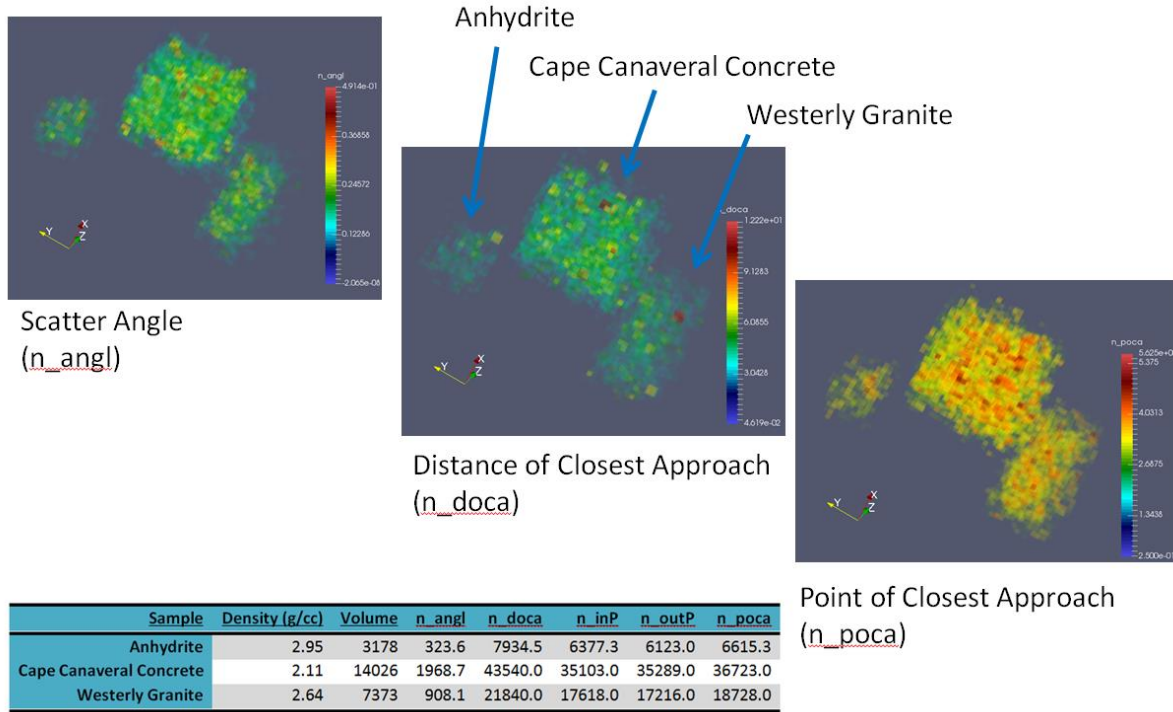


**Figure 12. Segmented scatter angle, DOCA and POCA values**

To simplify data processing, the measurement volume was partitioned into 130 x 130 x 120 centimeter voxel bins. For each muon strike, POCA point is evaluated to determine its corresponding voxel bin. Then, the POCA, DOCA, and scatter angle accumulators for that voxel bin are updated such that: (a) the POCA accumulator is increased by 1.0, (b) the DOCA accumulator is incremented based on the DOCA value, and (c) the scatter angle accumulator is incremented by the scatter angle in radians.

## 2.5. Results

Results from accumulator technique for each rock sample are shown in Table 1. The Angle values in Table 1 are the sum of the scatter angles in radians within the segmented volume for each sample. In like manner, the DOCA and POCA results in Table 1 are the summed values for the segmented volume. The raw accumulated values are then divided by the measured volume for each sample and are tabulated in Table 2. Plotted results from Table 2 are shown in Figure 13 and Figure 14.

**Table 1. Tabulated Muon Reconstruction Results**

<u>Sample</u>	<u>Sample Volume</u>	<u>Angle</u>	<u>DOCA</u>	<u>POCA</u>
Cape Canaveral Concrete	14026	1968.7	43540.0	36723.0
Salt (fractured)	11012	1009.4	26747.3	22278.2
Salt (intact)	20529	2241.4	64512.8	55372.0
Berea Sandstone	17042	1760.2	55428.8	47200.5
Austin Limestone	9640	987.3	27539.5	22740.4
Marble	7288	786.1	21855.7	18361.5
Westerly Granite	7373	908.1	21840.0	18728.0
Anhydrite	3178	323.6	7934.5	6615.3
Pyrite	2825	314.0	8457.4	7247.4

**Table 2. Muon Reconstruction Results**

<u>Sample</u>	<u>Density</u>	<u>Angle/V ol</u>	<u>DOCA/V ol</u>	<u>POCA/V ol</u>	<u>Angle %Err</u>	<u>DOCA % Err</u>	<u>POCA % Err</u>
Cape Canaveral Concrete	2.1 1	0.140	3.104	2.618	-0.933	0.471	0.241
Salt (fractured)	2.1 2	0.092	2.429	2.023	-0.957	0.146	-0.046
Salt (intact)	2.1 4	0.109	3.143	2.697	-0.949	0.468	0.260
Berea Sandstone	2.2 4	0.103	3.252	2.770	-0.954	0.452	0.236
Austin Limestone	2.4	0.102	2.857	2.359	-0.957	0.190	-0.017
Marble	2.5 6	0.108	2.999	2.519	-0.958	0.171	-0.016
Westerly Granite	2.6 4	0.123	2.962	2.540	-0.953	0.122	-0.038
Anhydrite	2.9 5	0.102	2.497	2.082	-0.965	-0.154	-0.294
Pyrite	5.0 1	0.111	2.994	2.565	-0.978	-0.402	-0.488

The results shown in Figure 13 and Figure 14 are inconclusive for the rock samples tested. It is interesting to note that the POCA and DOCA results show similar results offset by a small bias. Another aspect of interest is the values for the fractured salt sample. The scatter angle, DOCA, and POCA values are all relatively lower than that of the intact (without fractures) salt sample indicating that the two have different densities. The fractured salt sample is slightly less dense than the intact salt sample but they are relatively close.

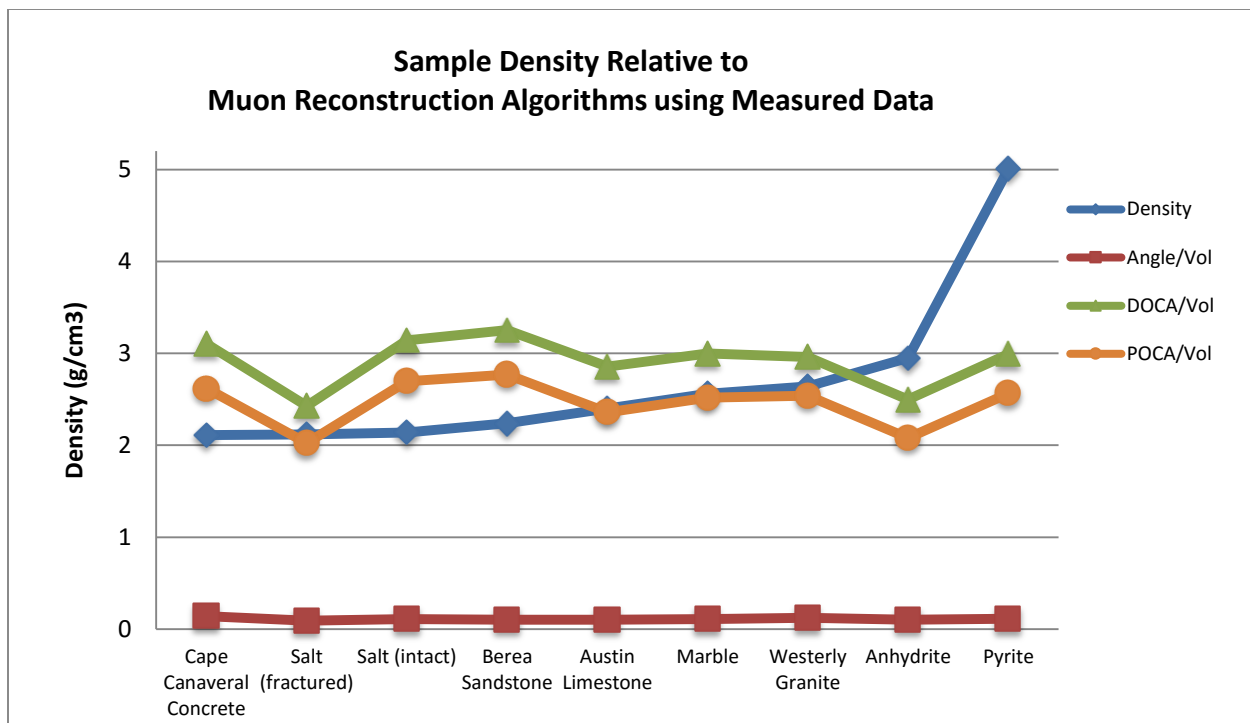


**Figure 13. Sample Density Relative to Muon Reconstruction Results**

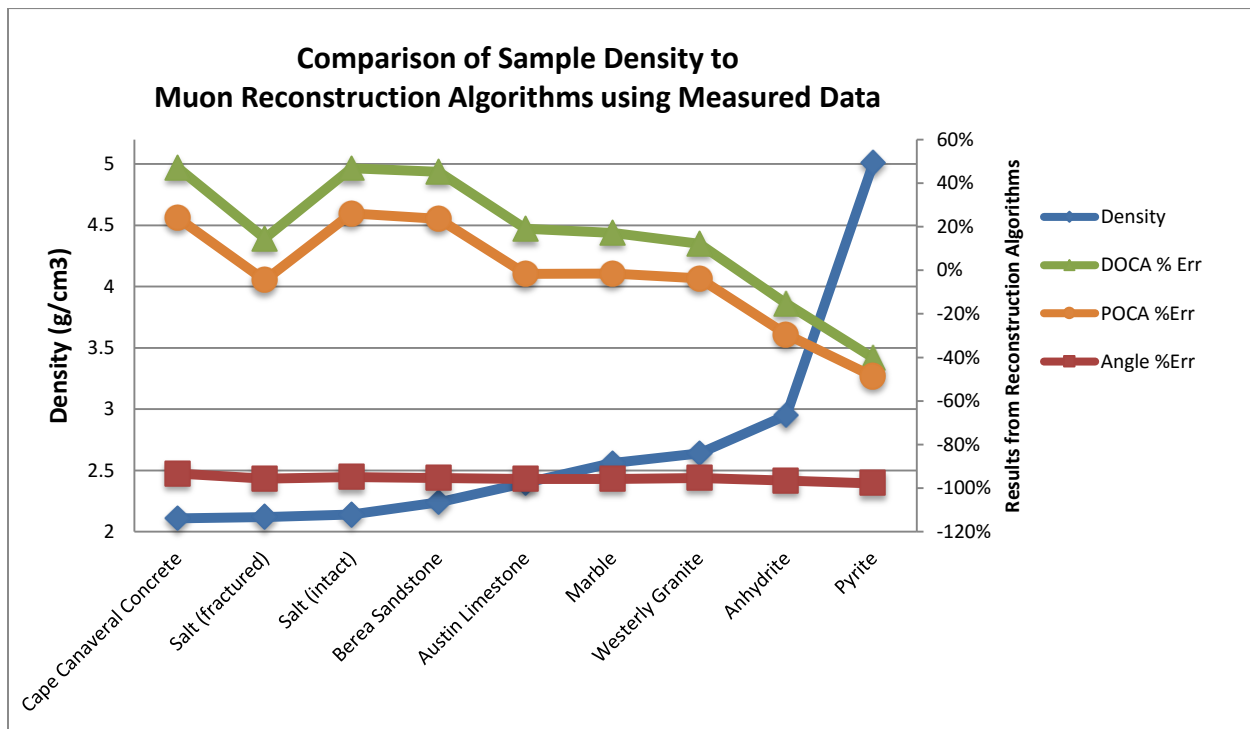


**Figure 14. Comparison of Sample Density Relative to Muon Reconstruction Results**

### 2.5.1. Synthetic comparison using MCNP6

Muon scattering through rock samples is simulated using MCNP6 (Monte Carlo N Particle version 6) for comparison with the real data described in the previous section. MCNP is a general purpose Monte Carlo N-Particle radiation transport code designed to track multiple particle types, including muons, over a broad range of energies (Gorley, et al. 2012). The code enables building the complex muon source model and a set of tallies that mimics the tomography measurements. Physics tables for muons in MCNP underestimate stopping power above  $\sim 100$  GeV (radiative contributions are not included), but are not anticipated to affect the tomography simulations since muon energy at the surface is typically on the order of a few GeV.

The cosmic muon source model in the MCNP simulation was based on the parameterizations from measured data compiled by Reyna (2008) to accurately sample the muon flux and energy spectrum as a function of incident angle. Figure 15 shows how the MCNP muon source model distribution agrees with surface muon flux plotted as a function of the scaling variable  $\zeta = p_\mu \cos(\theta)$  when each dataset is scaled by a factor of  $1/\cos^3(\theta)$ . Application of the Reyna parameterization fits multiple measured data sets. Figure 16 shows how the MCNP muon source model distribution agrees with surface muon flux plotted as a function of the scaling variable  $\zeta = p_\mu \cos(\theta)$  but without scaling each dataset. In the case of Figure 16, the dependence of muon flux on zenith angle is apparent. Figures 15 and 16 clearly demonstrate the effectiveness of using MCNP to simulate muon flux.

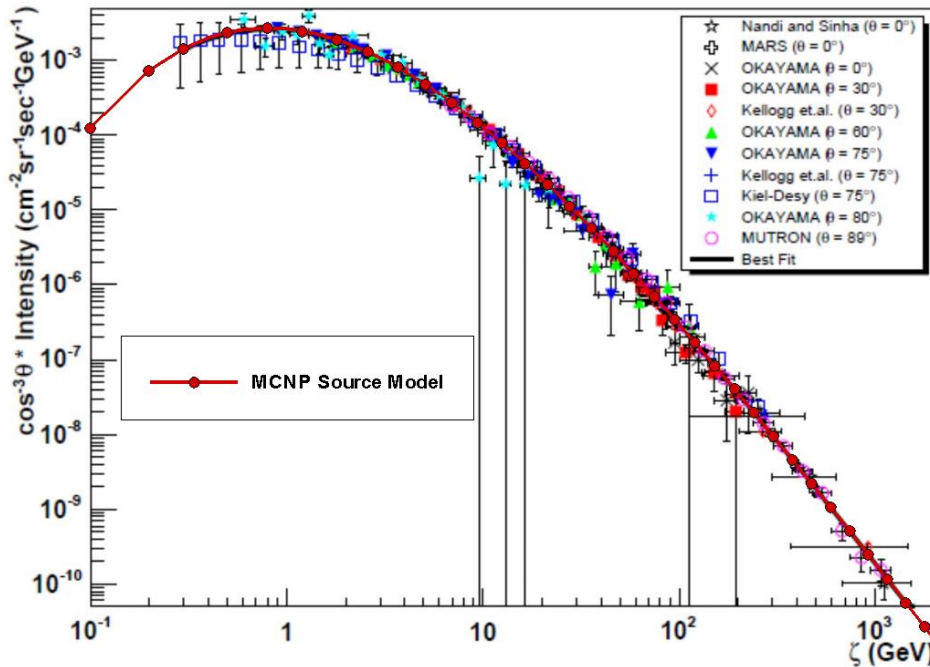


**Figure 15. MCNP muon source model distribution (red dots and solid red line) overlaid on Figure 3 from Reyna (2008).**

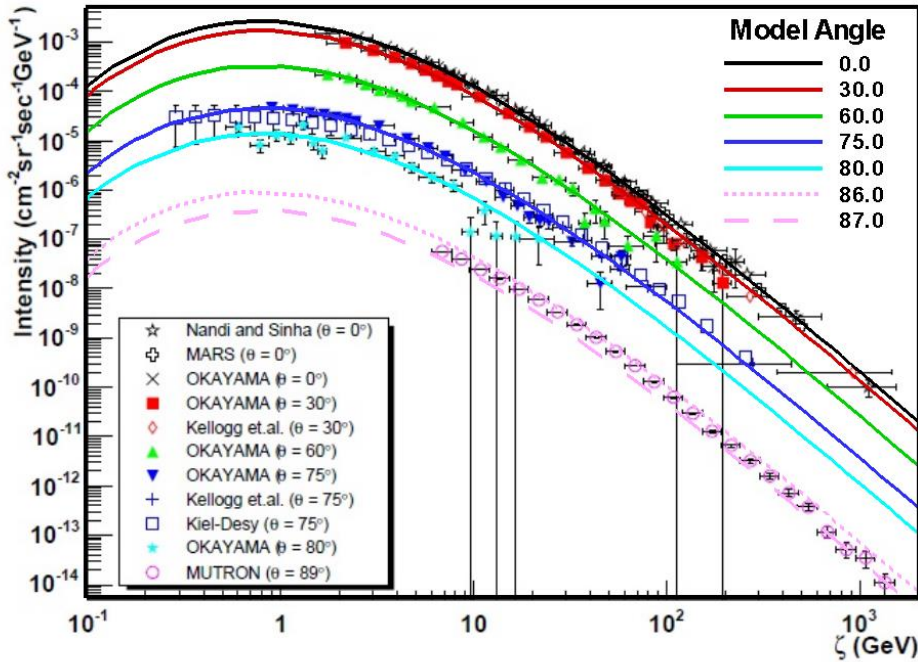


**Figure 16. MCNP muon source model distribution (solid lines) overlayed on Figure 2 from Reyna (2008). Note that the MUTRON measurements cited at 89° were collected from 86° to 90° (Matsuno et al., 1984).**

The MCNP simulations used a PTRAC output file to track muon state at the inner surfaces of the upper and lower planes of the simulated detector to allow post processing of the simulated data in the same manner as the measured data.

### 2.5.2. Simulation Results

Results show strong comparison between experimental and simulated data. A series of three tomographic scans were performed on several geological samples, summarized in Table 3. The locations of the samples in the simulations were estimated from the measurement results.

**Table 3. Geological sample summary for measurements and simulations.**

Tomography Scan	Sample Number	Sample Material	Simulated Density [g/cm <sup>3</sup> ]
1	1	granite	2.64
1	2	concrete	2.11
1	3	anhydrite	2.95
2	1	salt	2.17
2	2	fractured salt	2.1483
2	3	sandstone	2.24
3	1	limestone	2.61
3	2	marble	2.56
3	3	pyrite	5.01

Processing of the simulated data to determine most likely scatter location for differing vectors is successful at identifying sample locations and edges. Most probable scatter location is determined by propagating upper and lower vectors into the detector volume and computing the point of closest approach. Scatter angle is computed from the dot product of the two vectors. Additionally, the muon track length density and scatter density through the voxelized sample region is computed. Figure 17, Figure 18, and Figure 19 show the scatter density per track length density in each simulation after 355 million muon histories, which corresponds to approximately 6 days of measurement. Filters have been applied to the voxels in each figure, and only those with track length density greater than  $0.012 \text{ cm/cm}^3$  and average scattering angle greater than 0.5 degrees are shown. As shown in the figures, edge detection and differentiation between rock sample and void regions in the tomography region are easily discriminated.

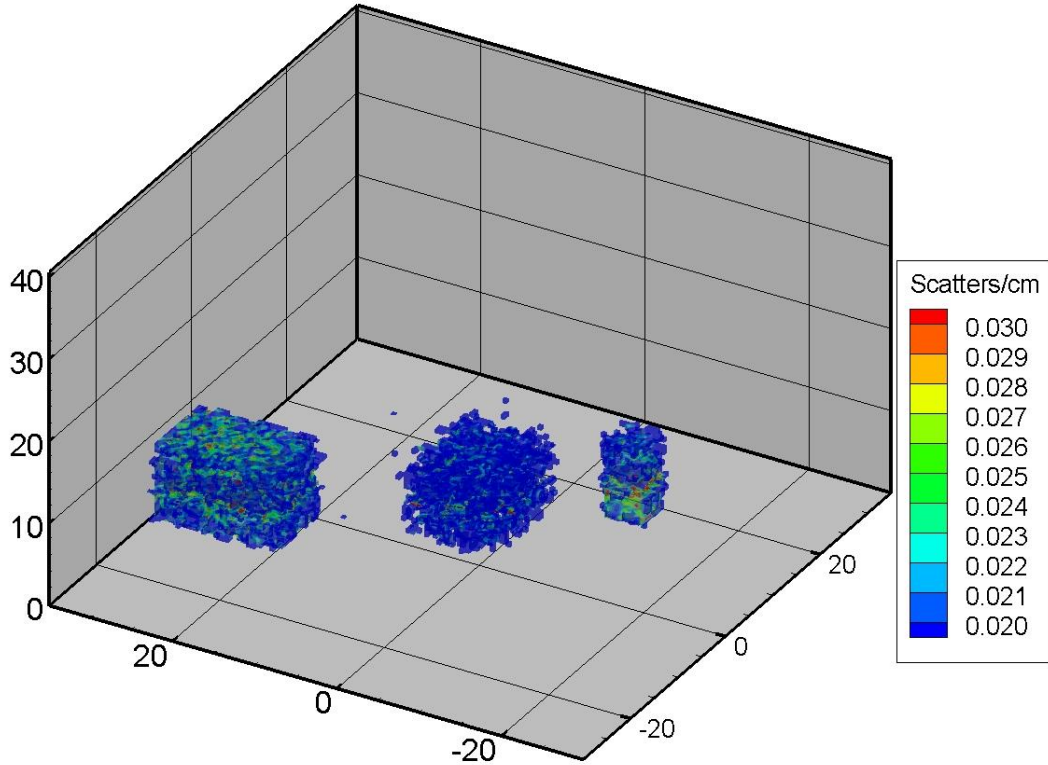


**Figure 17. Simulation of muon tomography scan of granite, concrete, and anhydrite samples. Voxels where scatter density per muon track length density for scatters greater than 0.5 degrees and  $0.012 \text{ cm/cm}^3$  of track length density are shown.**

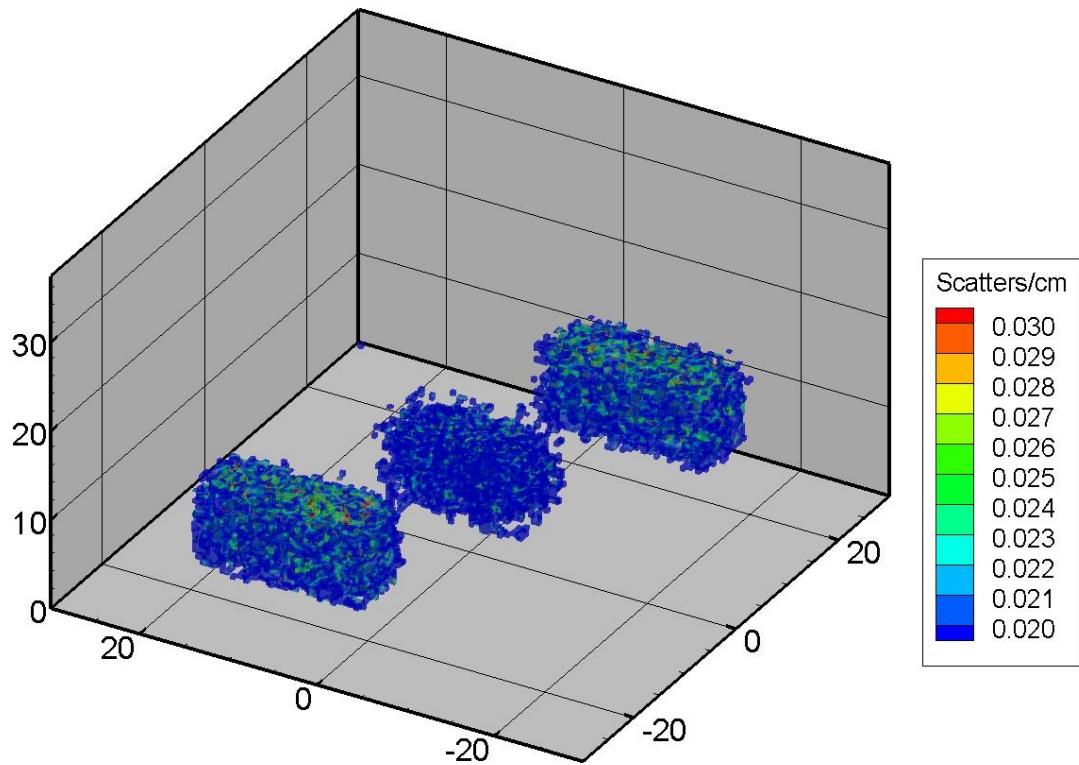


**Figure 18. Simulated muon tomography scan of salt, fractured salt, and sandstone samples. Voxels where scatter density per muon track length density for scatters greater than 0.5 degrees and 0.012 cm/cm<sup>3</sup> of track length density are shown.**

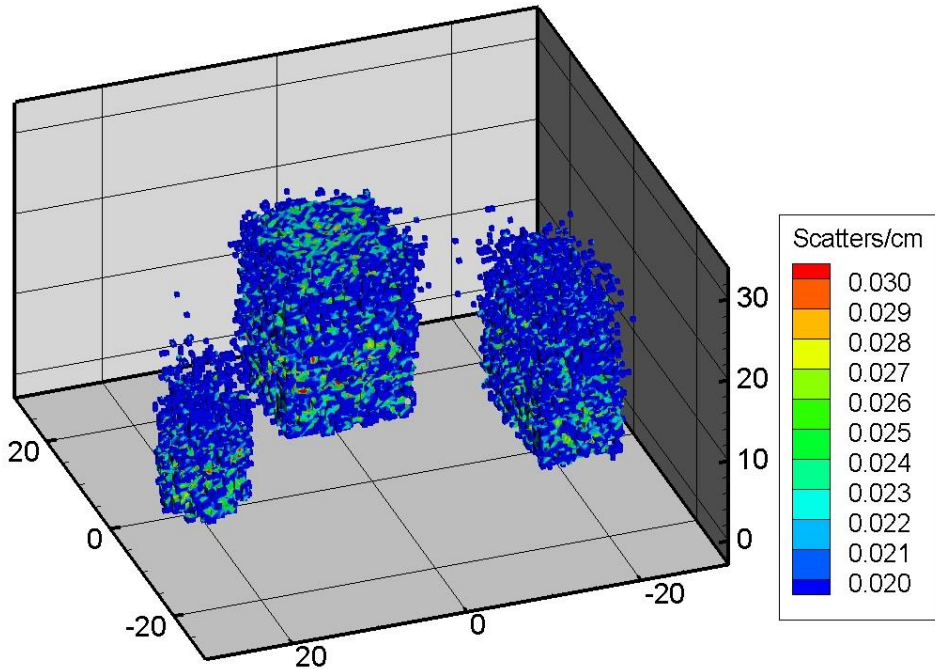


**Figure 19. Simulated muon tomography scan of limestone, marble, and pyrite samples.**  
**Voxels where scatter density per muon track length density for scatters greater than 0.5 degrees and 0.012 cm/cm<sup>3</sup> of track length density are shown.**

Density determination via the simulated results has been not been successful. With the exception of the pyrite sample at 5.01 g/cm<sup>3</sup>, the sample densities are all within 10-15%. There has been no observable correlation in the simulated data within each sample volume between sample density and muon track length density, muon scatter density, average muon scatter angle, muon scatter angle distribution, muon scatter density per muon scatter angle, or average muon track length to scatter.

## 2.6. Conclusions

Muon scattering tomography can be used to distinguish between materials of different densities, provided there is sufficient density contrast. Results from these experiments using the analyses discussed herein are inconclusive. However, rock density does show a linear relationship with muon scattering density per rock volume for these samples when this ratio is greater than 0.10.

Going forward, volume segmentation should be implemented using known measured locations of each rock sample to isolate error due to segmentation. This is easily done since the locations and sizes of the samples are clear in the tomographic images. For both methods, better results may be obtained by flat fielding the detector results using data acquired from an empty detector accumulated over the same time as the rock experiments. Attempts should be made to measure materials of greater density variations but of the same volume.

## 2.7. Acknowledgements

Sandia National Laboratories is a multi-mission laboratory managed and operated by Sandia Corporation, a wholly owned subsidiary of Lockheed Martin Corporation, for the U.S. Department of Energy's National Nuclear Security Administration under contract DE-AC04-94AL85000.

## 2.8. References

- Alvarez, Luis W., Jared A. Anderson, F. El Bedwei, James Burkhard, Ahmed Fakhry, Adib Girgis, Amr Goneid, Fikhry Hassan, Dennis Iverson, Gerald Lynch, Zenab Miligy, Ali Hilmy Moussa, Mohammed-Sharkawi, and Lauren Yazolino, (1970). *Search for Hidden Chambers in the Pyramids*, Science **167**, 832-839.
- Borozdin, K.N., G.E. Hogan, C. Morris, W.C. Priedhorsky, A. Saunders, L.J. Schultz, and M.E. Teasdale, (2003). Surveillance: Radiographic imaging with cosmic-ray muons, *Nature* **422**, 277, doi: 10.1038/422277a.
- Goorley, T., M. James, T. Booth, F. Brown, J. Bull, L. J. Cox, J. Durkee, J. Elson, M. Fensin, R. A. Forster, J. Hendricks, H. G. Hughes, R. Johns, B. Kiedrowski, R. Martz, S. Mashnik, G. McKinney, D. Pelowitz, R. Prael, J. Sweezy, L. Waters, T. Wilcox, T. Zukaitis, (2012). *Initial MCNP6 Release Overview*, Nuclear Technology, **180**, pp 298-315.
- Nagamine, K., M. Iwasaki, K. Shimomura, and K. Ishida, (1995). *Method of probing inner structure of geophysical substance with the horizontal cosmic ray muons and possible application to volcanic eruption prediction*, Nucl. Instrum. Meth. **A356**, 585-595, doi: 10.1016/1068-9002(94)01169-9.
- Reyna, D., (2008). *A Simple parameterization of the cosmic-ray muon momentum spectra at the surface as a function of zenith angle*, hep-ph/0604145v2.
- Matsuno, S. et al., (1984). *Cosmic-ray muon spectrum up to 20 TeV at 89° zenith angle*, Phys. Rev. D. **29**, 1.
- Schultz, Larry Joe, (2003). *Cosmic Ray Muon Radiography* (Doctoral dissertation). Retrieved from ResearchGate.
- “ParaView (2016) is an open-source, multi-platform data analysis and visualization application.”  
<http://www.paraview.org/>

### 3. USING MUON FLUX TO DETECT A VOID IN ROCK

Another part of this work was aimed at imaging a vertical shaft from inside a tunnel to assess the ability to image a relatively small void space within a large volume of rock and estimate overburden from muon flux attenuation. The highly penetrating nature of high energy muons makes them useful for this application. Other useful parameters are listed below.

1. Muon flux:
  - At sea level the muon flux is approximately 10,000/min/m<sup>2</sup> with mean energy ~3 GeV for muons that are traveling vertically downward
  - Increases with elevation
  - Decreases rapidly with angle from zenith (vertical) by  $\sim \cos(\theta)^2$
  - Decreases ~1 order of magnitude/1.5 km.w.e. depth (Mei and Hime, 2006)
    - 1 km.w.e. = 105 g/cm<sup>2</sup> (depth \* density = interaction depth)
2. Muons can penetrate ~1.9 meters of iron, 15 meters of water, and 12.5 kilometers of air
3. Muon energy
  - a. Higher energy muons have greater depth of penetration
  - b. Higher zenith angles (near horizontal) have higher energies
4. Resolution improves with increased number of muons and imaging capabilities

A 4'x4' drift tube detector was placed in a tunnel in Albuquerque, New Mexico to image a 0.9 m (36") diameter vertical ventilation shaft through about 50 m (163' slant depth) of granite. This is equivalent to ~130 km.w.e. so only high energy muons will reach the detector. Four sets of data were collected from 3/25/16 to 9/12/16. The data sets were for different orientations and locations of the detector: 1) vertically oriented outside the tunnel near the tunnel entrance (e.g. open sky or flat field measurements), 2) vertically oriented inside the tunnel (direct overburden measurements), 3) horizontally (zenith angle = 58°) oriented outside the tunnel near the tunnel entrance (e.g. rotated open sky or flat field measurements), 4) horizontally (zenith angle = 58°) oriented inside the tunnel (target measurements). A zenith angle of 58° was chosen so that a vector from the center of the detector should intersect the ventilation shaft at a distance half-way between the tunnel floor and the ground surface as shown in Figure 20.

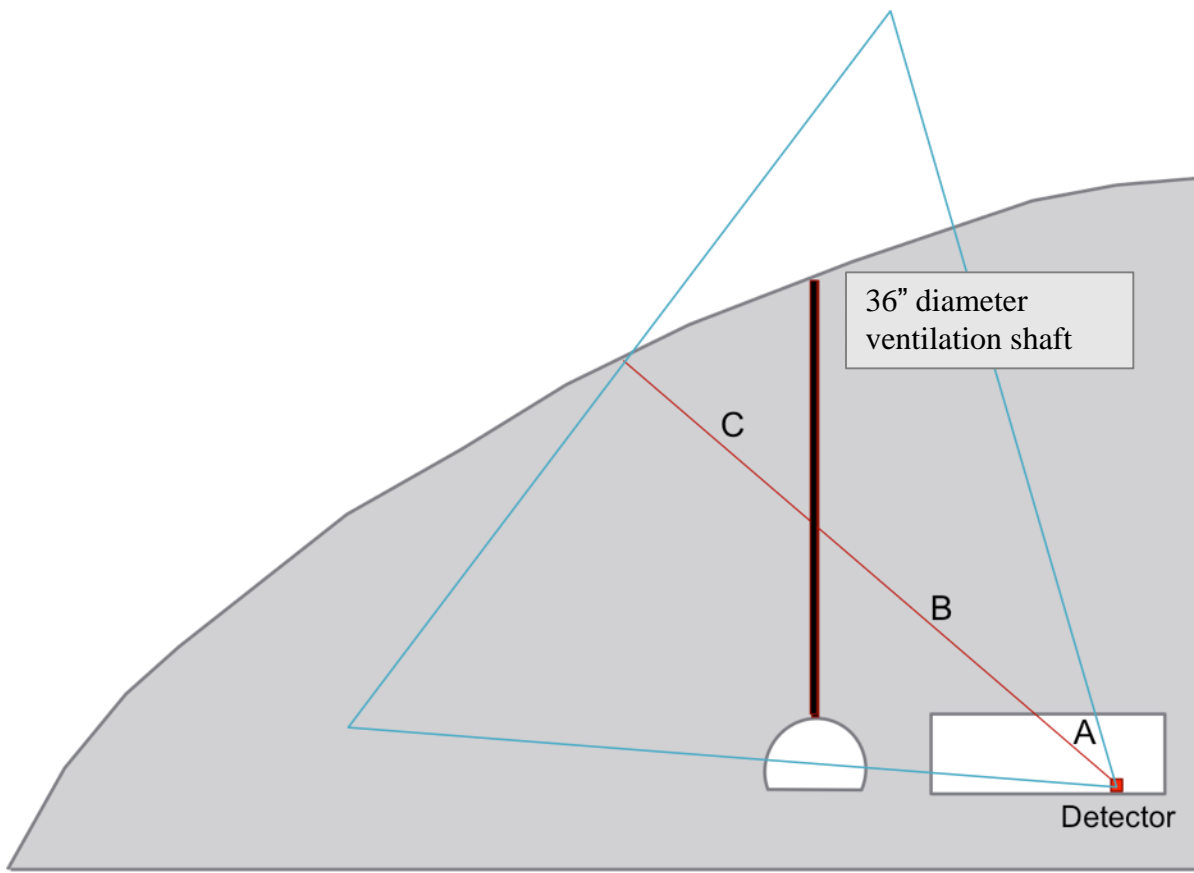


**Figure 20. Schematic of muon detector pointing at ventilation shaft from inside a tunnel.**

The gray area represents the granite rock with sloping elevation. The blue triangle represents the acceptance angle of the detector and the red line represents a vector from the center of the detector. Drawing not to scale.

Results from data images are ambiguous but muon attenuation agrees as expected from theory. Figure 21 is the muon attenuation surface by angle relative to the detector for data set 4) horizontally (zenith angle =  $58^\circ$ ) oriented inside the tunnel (target measurements). Ignoring the artifacts around the edges of Figure 21, the results quite similar to the elevation changes of the ground surface within the acceptance angle of the muon detector. The elevation of the ground surface is highest directly above the detector and decreases away from the detector in the direction towards the ventilation shaft. The trough-like area on the right of Figure 21 is also in the location of a lower elevation drainage feature seen on the ground surface. Likewise, the muon attenuation surface by angle relative to the detector for data set 3) vertically oriented inside the tunnel is quite similar to the elevation changes of the ground surface for that case. The muon attenuation surface for the vertical case inside the tunnel is shown in Figure 22. The ground surface elevation above the detector for the vertically oriented case has less elevation change in this area.

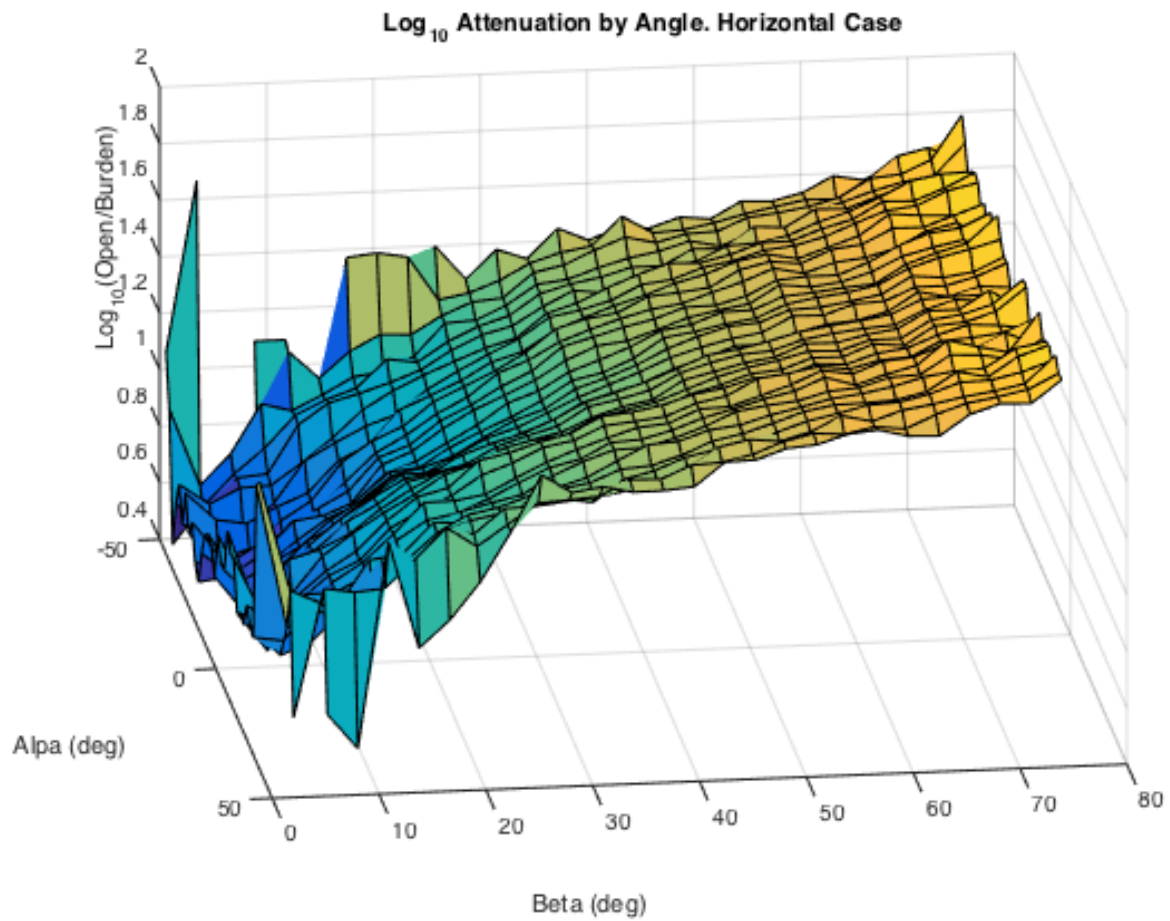


**Figure 21. Muon attenuation surface by angle relative to the detector for data set 4) horizontally (zenith angle = 58°) oriented inside the tunnel (target measurements). Figure 21 is oriented relative to Figure 20.**

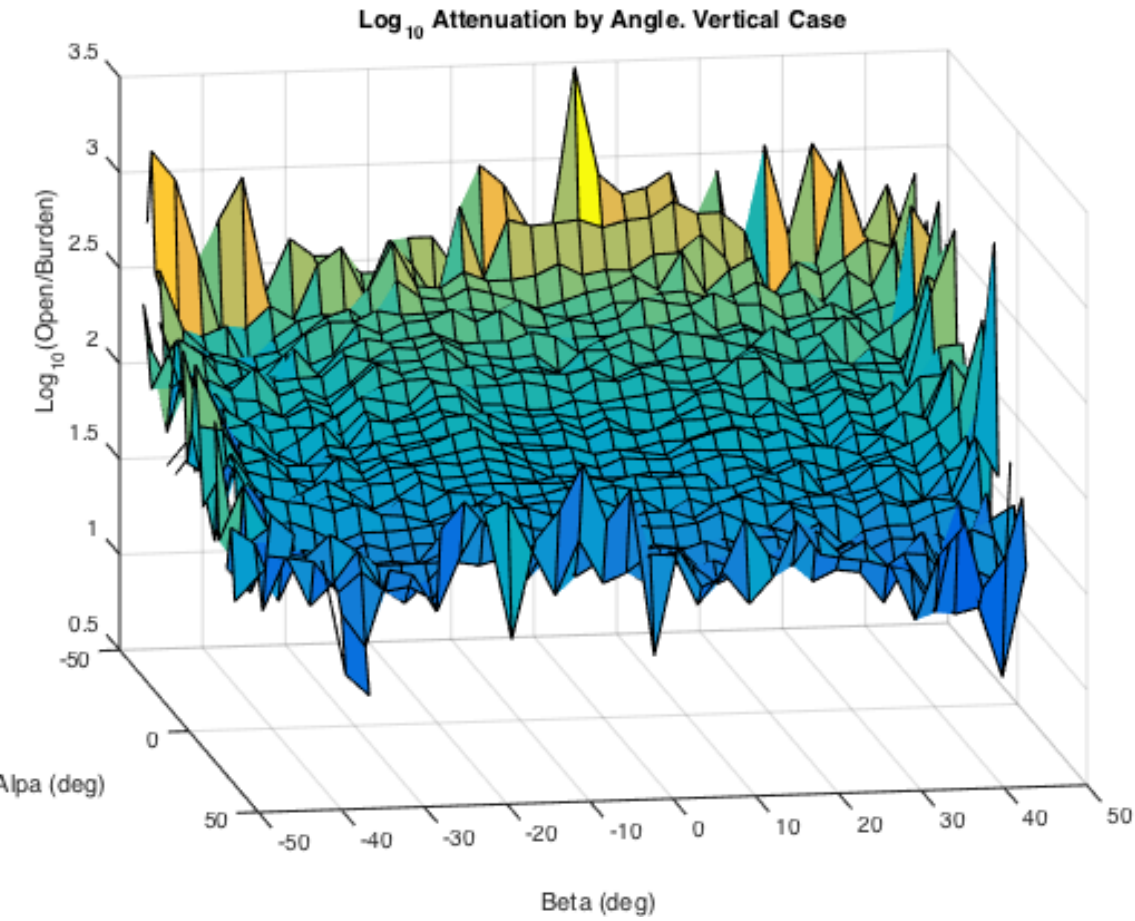


**Figure 22. Muon attenuation surface by angle relative to the detector for data set 3 vertically oriented inside the tunnel. Figure 22 is oriented relative to Figure 20.**

For telescopic mode using this detector, the resolution is on the order of about one meter but depends on the angular resolution and the distance between the target and the detector. Since the ventilation shaft was on the order of the resolution of this detector, it may not be detectable under these circumstances. Future work should ensure the target of interest is much larger than the resolution ability of the detector to definitively assess muon capabilities to image the target. Restrictions with this work prevented optimal survey design for this assessment. Additionally, further image processing techniques could be explored to improve the image results.

## 4. MEASURING MUON DIRECTION

### 4.1. Abstract

A muon trajectory tracker was developed using three stacked large square (76cm x 76cm) panels of polyvinyltoluene (PVT) scintillator plastic instrumented with photomultiplier tubes (PMTs) mounted at the corners. The panels are mounted in parallel on an aluminum frame that allows for simple adjustment of angle position, rotational orientation and separation distance between the panels (viewing angle). The responses of all PMTs in the system are digitized simultaneously at a sub-nanosecond sample rate. Custom LabView software was developed to adjust collection settings and implement event rejection based on the number of panels that detected a scintillation event within the 400 nanosecond (ns) record. The relative responses of the PMTs are used to triangulate the position of scintillation events within each panel. The direction of the muons detected in the system can be tracked using the panel strike order. The direction detection is experimentally verified by examination of the forward/reverse relationship when oriented vertically and when oriented horizontally with one side facing the Manzano mountain range. Methods for triangulation by time-of-flight (TOF) and PMT magnitude response are discussed. A grid of holes in the scintillator covering was used to generate calibration datasets with short pulses from a light emitting diode (LED) that emits near the center wavelength of the PVT response spectrum. Pulses were adjusted to a width and amplitude that mimics muon scintillation events and data was recorded using the muon data collection instrumentation and software. A Gaussian process regression (GPR) machine learning tool was implemented to learn the relationship between normalized PMT response features and x and y positions from the calibration dataset. A separate LED dataset collected on the grid was used to examine the predictive capability of the trained GPR fit in various locations on the PVT panel. The resolution is analyzed using different numbers of PMTs and low versus high PMT sensitivities. Non-uniform reflective coating around the PVT panels and asymmetries in PMT coupling efficiency cause disparity in resolution in symmetric positions about the center.

### 4.2. Introduction

Muons are subatomic particles created by cosmic rays interacting with the upper atmosphere and neutrino interactions within the earth. High-energy muons can penetrate several kilometers into the crust of the Earth. These particles are more sensitive to density variation than other phenomena, making them interesting for subsurface characterization. Muon absorption rates depend on the distance traveled and on the density of the materials they travel through. Density

variations of the materials between the muon source and detector can be measured from the muon flux rate at different locations, much like a CAT scan. Muons were used in 1955 to measure the overburden of a tunnel (George E. P., 1955), which provided a faster and more cost effective method than drilling for depths greater than 15.24 m (50 ft). Alvarez et al. (1970) used muons to search for hidden chambers within the Egyptian pyramids. The results of Alvarez's work proved that the Pyramid of Khafre (the second pyramid) does not have any hidden chambers like those in the Pyramid of Khufu (the first pyramid). Nagamine et al. (1995) pioneered the technique of using muons to investigate volcanoes. Interest in using muons for noninvasive imaging applications has expanded in recent years (Borozdin et al. 2003, Jourde et al., 2013, Gibert et al., 2010, Tanaka et al. 2010, Taira et al. 2010).

One of the most common architectures of muon trajectory detectors employs strips of scintillator material (Clarkson et. al., 2014, Lesparre et al. 2012, Marteou et al. 2014, Riggi et al. 2013, Uchida et al. 2010) arranged in orthogonal rows with a separate PMT monitoring scintillation events on each strip. In these "hodoscope" systems, X and Y positions are tracked by which set of PMTs respond at the "same" time. This method allows for tracking the x and y position of each muon with resolution limited by the size of the strips and number of PMTs used. To avoid space congestion, light can be guided from each strip to each PMT using fiber optic lines. These systems work reliably but can quickly become mechanically complex and costly as resolution is improved and trajectory tracking is implemented. Another muon tracking system uses a grid of drift chamber detectors. In drift chamber systems, the muon track resolution is improved by determination of the best straight line fit to the possible tracks from the chamber activation pattern of a given event (Pesente et al., 2009). Drift chamber muon tomography systems can be very accurate but are heavy and require many channels.

A recent simulation study (Aguiar et al. 2015) suggests the feasibility of muon detection systems similar to gamma cameras (Anger 1958) that use large sheets of plastic scintillator material with a low number of PMTs. For a given resolution, these single plastic scintillator slabs with a sparse grid of PMTs can be significantly less expensive and complex than their hodoscope counterpart. The approximate x and y positions of scintillation events are interpolated from relative activations of the surrounding grid of PMTs. The detected strike positions in gamma camera architectures like these are more like probability clouds than precise pixel resolution. With multiple stacked panels, a best fit straight line technique similar to that of the drift chamber method could be employed to improve track resolution. Panels can be added to the system with low additional cost relative to layer addition in scintillator strip methods. Panels could also be configured into two separate stacks on the same guide rails to image items between stacks by angle deflection from one stack to the next similar to what (Schultz et al. 2004, Borozdin et al. 2005) accomplished with drift chambers. The system developed herein uses the scintillator slab method with three panels stacked on a frame that allows for simple adjustment of view angle and orientation and a regressive machine learning algorithm for position cloud localization. PMTs are mounted on the corners of the PVT scintillator plates rather than the standard orthogonal grid to improve modularity in panel positioning and addition of more panels. Techniques and derivations are discussed for event localization and empirical data and practical observations are presented.

Much of the work in muon radiography and tomography (Alvarez, 1970; Borozdin et al. 2003; Lesparre et al., 2010; Marteau et al., 2012; Nagamine et al., 1995; and Tanaka et. al, 2003;) has been done using muons traveling at low zenith angles where contamination from muons traveling in the opposite direction from the target direction are negligible. For example, horizontally traveling (zenith angle = 90 degrees), muons will hit the detector from opposite directions, contaminating the image trying to be produced assuming muons are coming from one side of the detector. With a sub-nanosecond sample rate and precise cross-channel synchronization (<5 picoseconds), the present system can determine the forward/reverse directionality of particles traveling through the panels and as such could greatly reduce image noise.

### 4.3. Materials

A modular muon detector is designed using three parallel solid panels of plastic scintillator. Each of the three scintillator panels are square, 76 cm x 76 cm and 2 cm thick (30" x 30" x 0.8"). The plastic scintillator consists of polyvinyltoluene and organic flours with a light output of 10,000 photons/MeV. The optimum scintillator wavelength band is between about 400 nm to over 500 nm with maximum emission at 425 nm. The rise time is 0.9 ns and the decay time is 2.1 ns with a pulse width of about 2.5 ns measured at full width at half maximum (FWHM). This plastic has properties of long optical attenuation length and fast timing that are important for this application.

ET Enterprises series 9266B 2-inch photomultiplier tubes (PMTs) are used to convert the light signals from scintillation into electrical signals. These PMTs are low cost, rugged, and stable for our applications.

#### 4.3.1. *Mechanical Description and Frame Assembly*

The PMTs are coupled to the chamfered corners of each scintillator panel. A fourth PMT may be added to the last corner to improve coverage of the scintillator and improve location resolution.

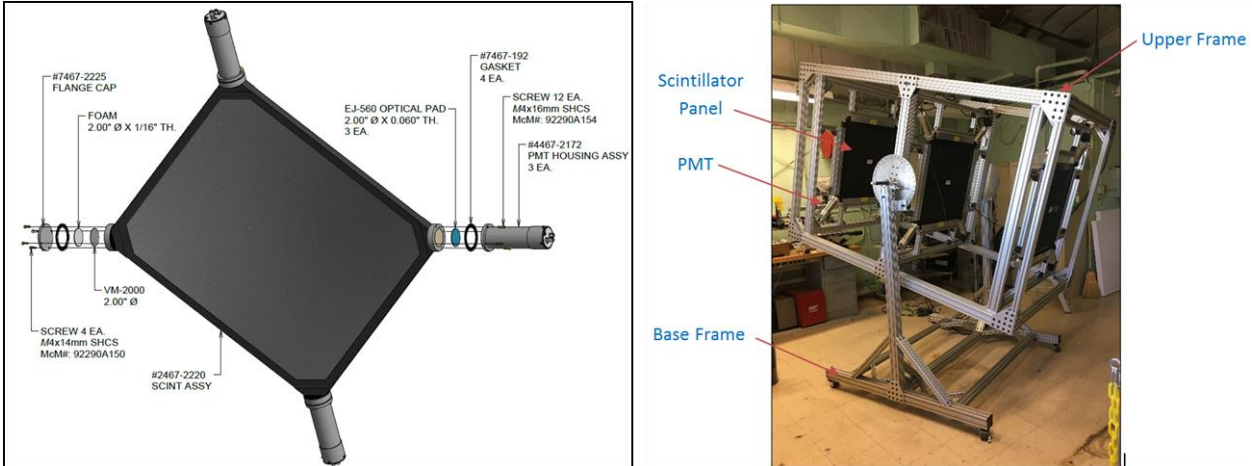


**Figure 23: Exploded view of scintillator panel assembly (Left) and configurable frame (Right).**

To minimize the loss of photons produced during a muon scintillation event, the PVT was covered with 0.001" thick commercial grade aluminum foil on all sides of the panel except for the PMT-accepting chamfers. The aluminum foil was then overlaid with a protective sheet of 0.03" black vinyl. Each corner of the PVT panel is chamfered to accept a single 9266B photomultiplier tube. The resulting spacing between PMT centers constitutes a square grid of side length 28 inches. In other words, adjacent PMTs have center-to-center spacing of 28 inches while cross-corner PMTs have spacing of approximately 39.6 inches. Originally, three PMTs per panel were attached to the chamfered section of the PVT using EJ-500 clear, colorless optical cement, with the fourth corner left blind. A fourth PMT was added to the blind corner for further investigation. EJ-500 was chosen because of its similar refractive index to the PVT scintillator panel (1.57 for the cement vs. 1.58 for the panel).

Each PVT/PMT subassembly is secured within a square frame that attaches to the upper frame. The scintillator panel assemblies are able to slide lengthwise along the upper frame interior, allowing the maximum conical viewing angle of the three scintillator panels to vary between 42 and 143 degrees. Such a viewing range corresponds to a minimum and maximum center-to-center panel spacing of 3.0 and 36.8 inches, respectively. Additionally, the upper frame can rotate relative to the base frame via a bearing assembly secured at its center. The panel normal relative to the floor can be varied in 5 degree increments through a full 360 degree tilt rotation.

The detector frame is constructed from primarily 6105-T5 aluminum extrusion commonly known by the brand name, 80/20. The geometry of the extrusion profile enables members to be fastened with threaded inserts known as T-Slots. Overall, the entire assembly stands at slightly over 111 inches tall when the panel normal is vertical and weighs approximately 750 pounds. In this vertical orientation, the maximum widths are 60 and 65 inches. The structure is designed to

be modular, with the ability to install additional panels and to reposition them easily. The framing follows a design intended to facilitate rapid modification for deployment in shelter-less environments (i.e. field deployments). The consequence of providing an option for exterior deployment is a highly rigid frame with load ratings suitable to withstand high force winds, provided that suitable ground anchoring has been achieved. In an indoor setting, the base frame accepts casters to enable easy movement. Because the upper frame is supported at the mass center, the detector can be repositioned in angle or rotational position by a single person.

#### *4.3.2. Electronics & Instrumentation*

The PMTs require high voltage (HV), low current power; depending on the desired sensitivity, the required voltage could range from 500 volts to 1500 volts direct current (DC). Small footprint high-voltage HVM2000/12P power supplies are mounted on the frame near each PMT. The voltage can be adjusted from 20v up to 2000v to set PMT sensitivities. The small power supplies are powered by a 12V line run along the detector frame and are connected to the PMTs using safe high voltage connectors (SHV). The sensitivity of each PMT is controlled by the excitation voltage provided by the HVM2000 power supply. Because each PMT has an independent power supply, each tube can be set individually.

The signal output of each PMT is connected to the data acquisition system through Bayonet Neill-Concelman connectorized coaxial cables (BNC) identical in length and construction. PMT outputs are electrical current pulses so the current must be converted to voltage for recording. Signals are each terminated with a  $50\Omega$  resistor and the voltage on the resistor is recorded with the digitizer.

The smarts of the detector are located on a computer cart holding a power supply, computer, monitor, and a data acquisition system (Figure 2). Data is recorded using three National Instruments PXIe-5160 digitizer cards mounted in a PXIe-1073 chassis. Collection parameters including trigger threshold, sample rate, record length, muon discrimination etc. are controlled with LabView. Unless otherwise specified, data presented here was collected at 1.25 gigasamples per second. With upsampling, the time resolution can be increased in post processing. Each event is triggered when the signal from one of the PMTs on the center panel crosses a user-defined threshold. Upon triggering, a simultaneous record of all PMTs in the system is recorded for 400 nanoseconds, 200ns prior to trigger and 200ns after trigger. The channels are synchronized to within 5 picoseconds. The record is saved if a set of user-defined conditions are met (i.e. if greater than 6 PMTs responded in the record).

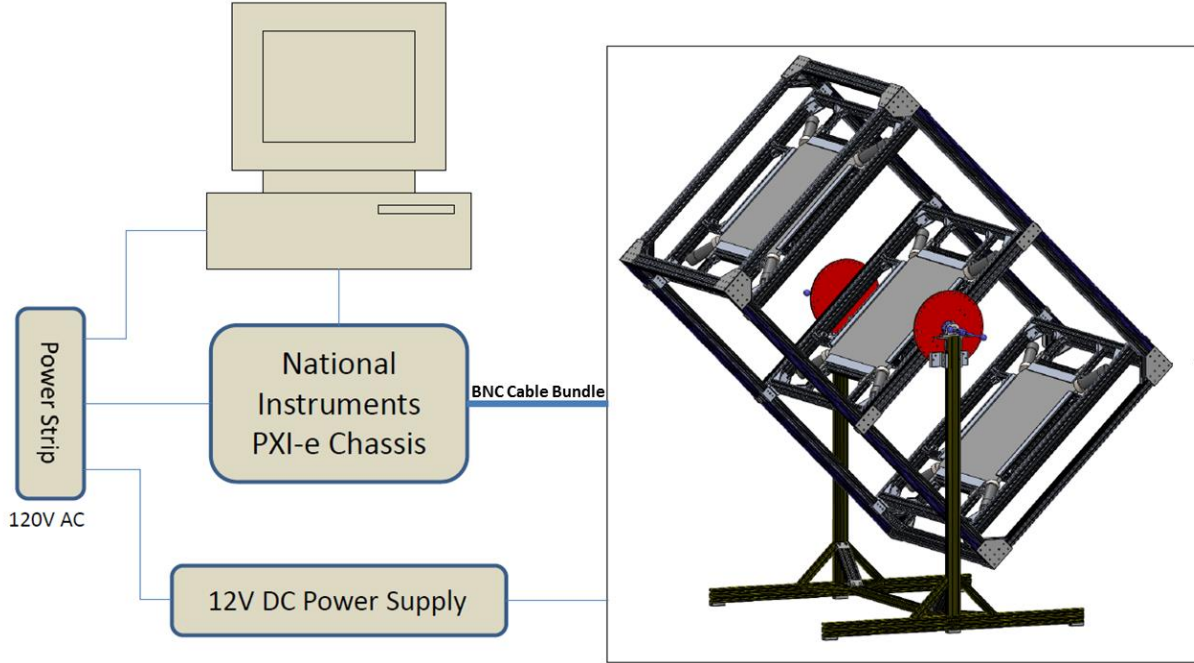


**Figure 24: Block schematic of instrumentation system and model of detector frame**

## 4.4. Single-Panel Interaction Position Determination

### 4.4.1. Triangulation by Timing

After a scintillation event, most photons take a long path with many reflections within the panel before reaching each PMT. Only a small portion of the photons produced will take a direct path to each detector which makes direct triangulation by timing difficult. In addition to the low signal, the transit time jitter of the PMT can introduce significant errors in time-of-flight (TOF) triangulation. However, with the assumptions that the direct path photons are detectable with the PMTs and that the error from transit time jitter is low, the position of the muon interaction point could be triangulated by direct derivation using the response timing of three PMTs. Knowing the refractive index of the scintillator plastic, differences in signal arrival time at each PMT can be converted to differences in distance traveled from the scintillation location. A system of equations can be solved for the x and y positions of the scintillation event (see below).

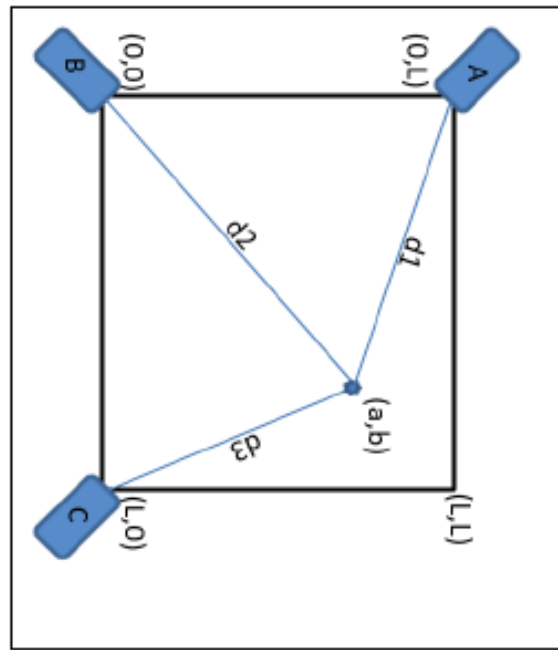


Figure 3. Derivation diagram for triangulation by difference in distance to each PMT

$$a = \frac{c^3 L t + c^2 L^3 - c^2 L t^2 + \sqrt{c} (c^3 L^4 t^2 - c^3 L^2 t^4 - 2c^3 L^4 t^3 + 2c^3 L^2 t^5 - 3c^2 L^6 t^2 + 4c^2 L^4 t^4 - c^2 L^2 t^6 + 2c^2 L^6 t^3 - 2c^2 L^4 t^5 + 2c^2 L^8 t^2 - 3c^2 L^6 t^4 + L^4 t^6) - cL^3 t - L^5 + L^3 t^2}{2(c^2 L^2 - L^4 + L^2 t^2)}$$

$$b = \frac{c^2 L^4 t - c^2 L^4 t^2 - c^2 L^5 - c^4 L^2 t - c^4 L^2 t^2 - c^2 L^6 t + c^2 L^4 t^3 + 2c^3 L^2 t^5 - 3c^2 L^6 t^2 + 4c^2 L^4 t^4 - c^2 L^2 t^6 + 2c^2 L^6 t^3 - 2c^2 L^4 t^5 + 2c^2 L^8 t^2 - 3c^2 L^6 t^4 + L^4 t^6) - cL^3 t - L^5 + L^3 t^2}{2(L^2 - L^4 + L^2 t^2)}$$

Where L is the edge length of the panel and a and b are respectively the x and y coordinates of the muon interaction point.

$$c = d_1 - d_2 = \sqrt{a^2 + (b - L)^2} - \sqrt{a^2 + b^2}$$

$$t = d_3 - d_2 = \sqrt{(a - L)^2 + b^2} - \sqrt{a^2 + b^2}$$

The equations in the above derivation (Figure 3) were used to triangulate a simulated muon strike from time-of-flight (TOF) information in the following way. Photon time of flight was simulated by the propagation delay through varying lengths of coaxial cable. Three different lengths of coaxial cable were connected to the output of a function generator with BNC connectors. The lengths were selected to coordinate with a given position on the panel (Figure 4). Short electronic pulses ( $\sim 30\text{ns}$ ) created on the function generator were sent through the BNC cables simultaneously using tee connectors. The other end of each cable was connected to one of the NI PXie-5160 cards on the muon data acquisition system. The muon data collection equipment was set with similar parameters to those for recording muon scintillations and pulses from the BNC cables were digitized. The data acquisition system samples fast enough to detect the delay through longer cables. Because these were repetitive pulses, random interleaved sampling was used to increase the sample rate to 5 gigasamples per second.

To compute differences in distance, the differences in time of arrival of the pulses on each channel were multiplied by the published propagation speed of an electric field in the coaxial cable ( $0.659c$ ) where  $c$  is the speed of light in vacuum. The distance differences were entered in the equations for  $a$  and  $b$  above and the simulated strike position was computed. An error of approximately 0.39 inches was calculated from the computed position to the known correct position.

The speed of electric field propagation in the coaxial cable used ( $0.659c$ ) is similar to the speed of light through the PVT scintillator plastic ( $0.633c$ ). This experiment demonstrates the efficacy of the TOF position triangulation derivation and of the muon recording instrumentation to resolve timing on the scale necessary. The 9266b PMTs in the present system have a transit jitter of 2ns which is too high to resolve position with this method reliably but with the addition of PMTs with lower transit time jitter, direct TOF triangulation may be possible.

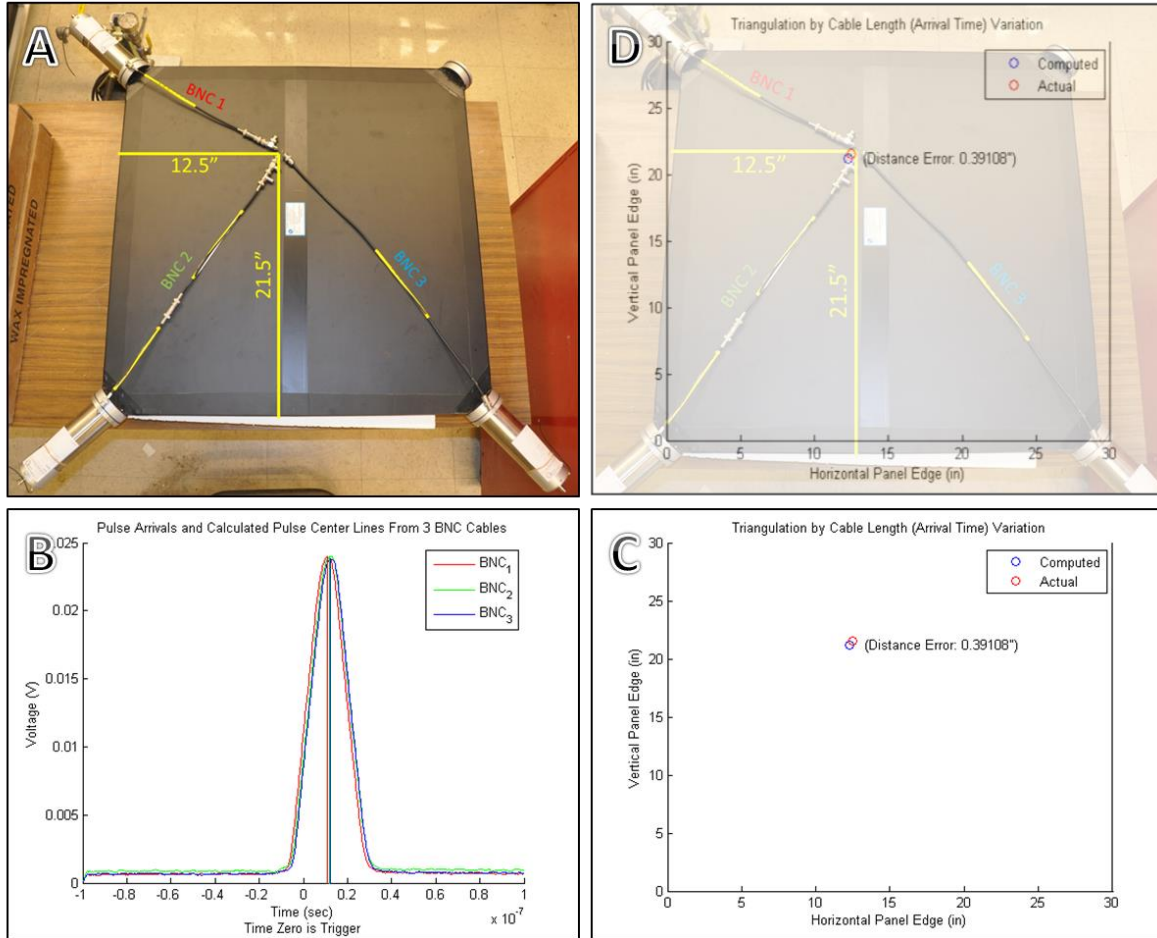


**Figure 25: (A) PVT scintillator panel with 3 PMTs attached at the corners. BNC cable intersection point is shown. (B) Pulses received on the 3 channels recorded. Small differences in arrival time can be seen. (C) Actual BNC cable intersection point compared to point computed from time differences. (D) Superimposed actual vs computed plot over scintillator panel.**

#### 4.4.2. Position calculation by Magnitude

The approximate position of the muon interaction point on the plastic scintillator can be determined using the magnitudes of the surrounding PMT responses. The effect of increasing gain and the number of PMTs used was examined.

The ideal way to both calibrate and determine the precision of the detector would of course be to use a muon beam generated from a particle accelerator. Not only would the exact strike position be known, but also the exact trajectory through the detector. Without a muon beam, calibration is limited to a panel by panel technique. One common discrete panel calibration/precision estimation technique used in gamma cameras is to use a source of ionizing radiation that will produce scintillation events in known locations about each panel. The PMT

responses can be recorded for known positions on the panel and the weighted sums can be adjusted so the computed position matches the known position of the source.

In lieu of a radiation source, a programmable flashing LED (470nm) was used to simulate scintillation events at known locations via a calibration panel. The calibration panel is constructed of 0.04"-thick ABS and has a 9x9-point grid of 1/16"-diameter holes drilled into the surface. Installation required that the black vinyl and aluminum foil was removed, exposing the bare PVT and displaying the construction of the opposite aluminum foil coating (Figure 5). The non-uniform surface of the aluminum foil prompted its replacement with Polyethylene Terephthalate, commonly known by the brand name Mylar®. In order to ensure the reflective properties of the material were the same on both sides of the PVT, Mylar sheeting was installed on the reverse side of the panel as well. Mylar has a reflectivity of approximately 0.98 versus 0.88 for aluminum foil. Its introduction into the system could thus be used to improve photon collection efficiency.

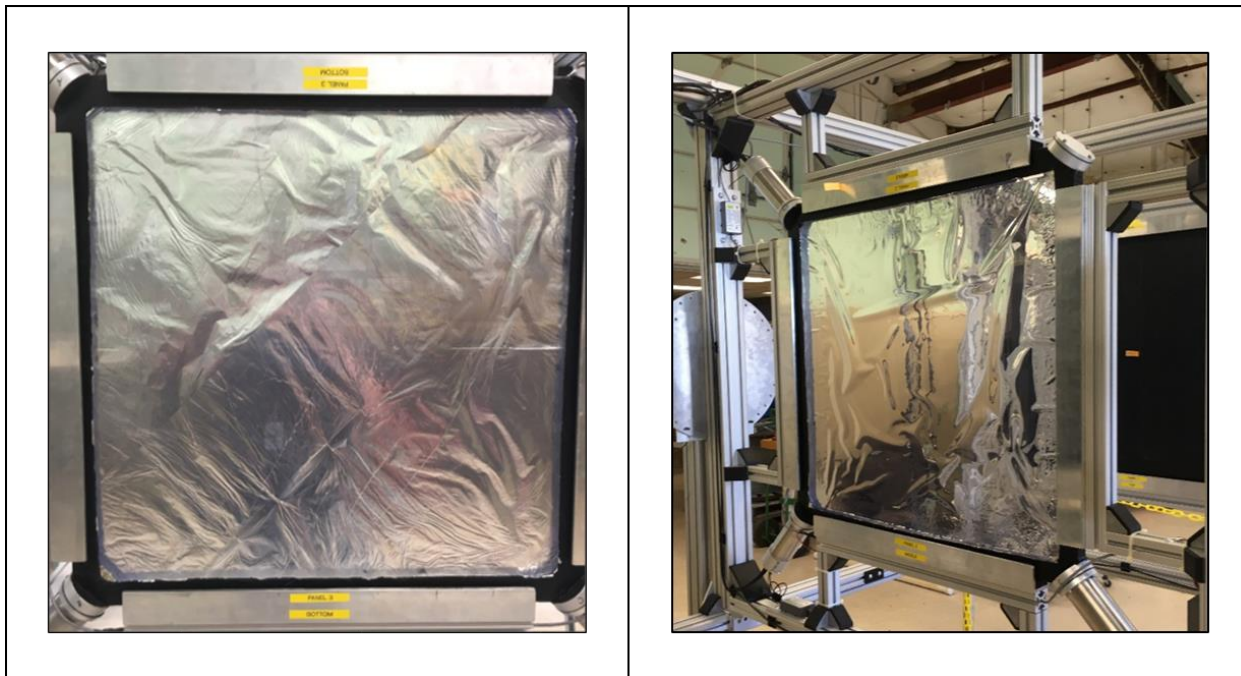


**Figure 26: Original industrial aluminum foil wrapping beneath the outer black plastic layer (Left) and Mylar wrapping installed with calibration hole grid sheet (Right).**

While the Mylar is more reflective than the original aluminum foil, it proved difficult to eliminate the waves created in the Mylar surface when installing the sheet with the scintillator panel already mounted on the framing system. The primary obstacle that arose was a bowing outward of the ABS sheet to which the Mylar was partially glued, which acted to create a series of large waves on the Mylar surface. A more effective method would have been to install the Mylar with the following techniques: 1) using a more rigid sheet of ABS or backer material and; 2) installing the Mylar before the assembly is secured in the framing system.

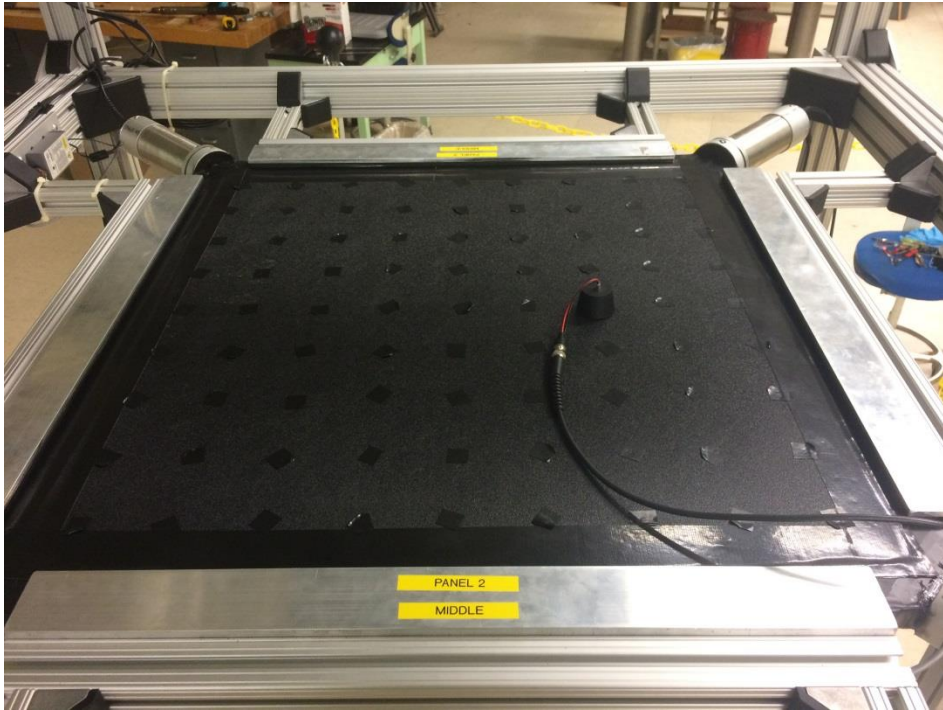


**Figure 27: Hole-grid calibration sheet installed on the PVT panel. The holes are covered with individual tabs of black electrical tape. The flashing LED is mounted in the rubber puck shown.**

The LED pulse parameters were set to nearly mimic the PMT response of a muon (i.e. pulse width of 50 ns, high voltage of 2.2v). As can be seen in Figure 6, all grid points in the calibration panel except for the point being interrogated are covered with standard electrical tape.

The PMT responses from the four corners of the panel were recorded with the muon data recorder hardware and software. Normalized magnitudes of the PMT responses and the known x and y positions were recorded for each flash of the LED. Data from two-hundred LED flashes from each of the 81 grid positions were used to train a Gaussian process regression machine learning tool in MatLab. A separate verification dataset of one-hundred more LED flashes were used to test the trained algorithm. The resultant calculated strike positions of the verification dataset were used to generate statistical Gaussian ellipses to estimate precision in various locations on the panel (Figure 7).

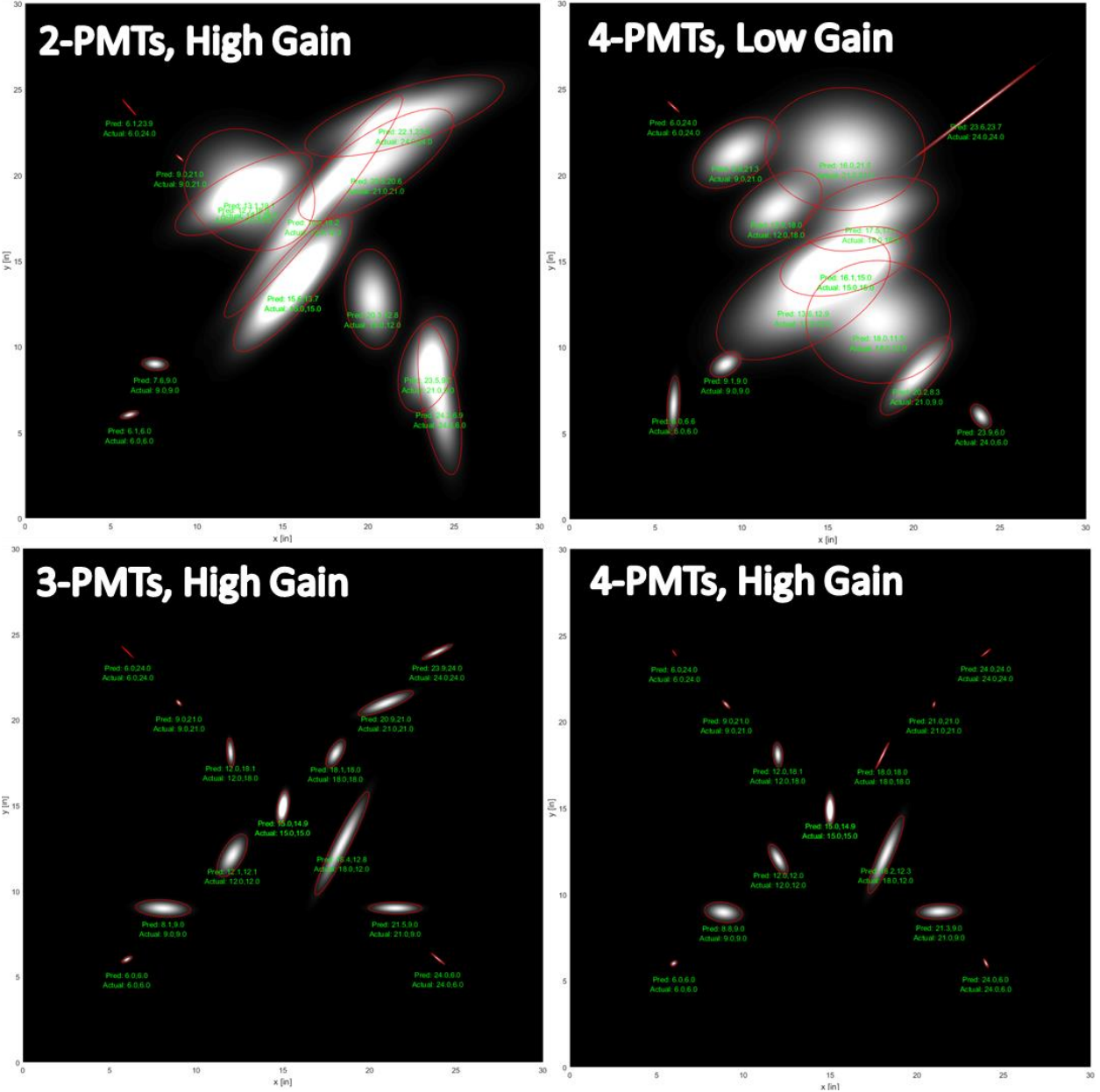


**Figure 28: Results of machine learning algorithm trained on calibration data, tested on separate data. Four configurations of PMTs are shown: With only 2 PMTs (Top Left), with 4 PMTs and low gain (Top Right), with 3 PMTs and high gain (Bottom Left), and with 4 PMTs and high gain (Bottom Right).**

Each red ellipse shows the elliptical radii where 90% of the predicted data falls for that position. The intervals were calculated based on the verification data set which was not used in training the RGP. The probability cloud for each point is shown in white and is normalized by its height for the display purposes of this plot. Table 1 shows the actual position, predicted center position, and long and short axis ellipse standard deviations of the computed verification data interaction point positions.

**Table 4. Tabulated machine learning performance data comparing results from using 3 PMTs against results from using 4 PMTs at the same gain setting.**

3PMTs, High Gain						4PMTs, High Gain					
Actual Position		Predicted Position		Standard Deviation		Predicted Position		Standard Deviation			
x	y	x	y	$\sigma_1$	$\sigma_2$	x	y	$\sigma_1$	$\sigma_2$		
6.000	6.000	6.003	6.001	0.074	0.152	5.983	6.000	0.056	0.091		
9.000	9.000	8.099	8.980	0.206	0.743	8.850	8.962	0.162	0.511		
12.000	12.000	12.086	12.063	0.263	0.621	12.004	12.029	0.117	0.398		
15.000	15.000	15.006	14.906	0.137	0.431	14.994	14.873	0.121	0.406		
18.000	18.000	18.049	18.031	0.178	0.423	18.015	18.036	0.021	0.370		
21.000	21.000	20.960	20.969	0.167	0.779	20.997	20.997	0.023	0.063		
24.000	24.000	23.918	23.958	0.094	0.462	23.989	23.985	0.004	0.177		
24.000	6.000	23.958	6.041	0.017	0.268	23.990	6.020	0.024	0.121		
21.000	9.000	21.498	8.997	0.150	0.713	21.283	8.999	0.185	0.602		
18.000	12.000	18.413	12.785	0.212	1.573	18.213	12.315	0.174	1.107		
15.000	15.000	15.006	14.906	0.137	0.431	14.994	14.873	0.121	0.406		
12.000	18.000	11.986	18.095	0.094	0.371	11.991	18.054	0.132	0.264		
9.000	21.000	9.003	20.988	0.037	0.096	9.012	20.991	0.051	0.116		
6.000	24.000	6.045	23.947	0.010	0.248	6.017	23.980	0.002	0.087		

With PMTs on each of the four corners, probability clouds in symmetric positions about the panel center should be of similar size. However, the system is sensitive to nonuniformities in the reflective coating around the PVT panel. In addition to a tendency to wrinkle and an unavoidable wrapping seam, the reflective aluminum foil develops slack which creates non-uniform space between the foil and the panel. A significant change in PMT response was observed during LED calibration when the foil is pressed flat compared to being left loose. Additionally, variances in coupling efficiency of the PMTs and uniformity of the panel may be a source of asymmetries in recorded data.

### 4.3. Multiple Panel Considerations

With the addition of multiple panels, trajectories can be computed, viewing angle can be adjusted, direction through the detector can be determined, and scintillation events that do not pass through all (or a given subset) of the panels can be rejected.

#### 4.3.1. Directional Determination

The direction of a muon through the system can be determined from the synchronized dataset of PMT responses. A constant fraction discriminator technique is used to determine the first arrival of the pulse from each PMT. The direction is determined by the strike order of the panels.

In the vertical position, the overwhelming majority of muons will be travelling downward and in the horizontal position, the nominal ratio is 50/50 in forward versus backward. The muon detector was configured with three PMTs per panel. The collection settings were set such that only events that struck all 3 panels were recorded. Three muon datasets were collected in vertical orientation and three were collected in East-West horizontal orientation. The direction of the muons for the datasets was computed and tabulated.

**Table 5. Tabulated data of direction of movement of muons through the detector in horizontal east-west orientation.**

Data Set	East Traveling Muons	West Traveling Muons	Total
<b>08092016153646</b>	578 (~42%)	793 (~58%)	1371
<b>08092016163640</b>	632 (~45%)	784 (~55%)	1416
<b>08092016173640</b>	220 (~43%)	296 (~57%)	516
<b>Total</b>	1430 (~43%)	1873 (~57%)	3303

Both the vertical and the horizontal muon datasets show consistent ratios of muons travelling forward versus backward through the detector. As expected, the vertical datasets show over 95% of muons travelling downward. The East-West horizontal datasets consistently show more muons traveling from west to east than in the opposite direction (Table 2) which is consistent with the geography of the surrounding area. The Manzano mountain range is a few miles east of the laboratory and partially obscures the view of the muon detector and likely attenuates the detected muon flux.

#### 4.3.2. Trajectory Tracking

Figure 8 shows a set of 100 random simulated muon tracks and a set of 100 computed muon tracks from real data. Computed strike locations were generated using the GPR fit model from the LED calibration data.

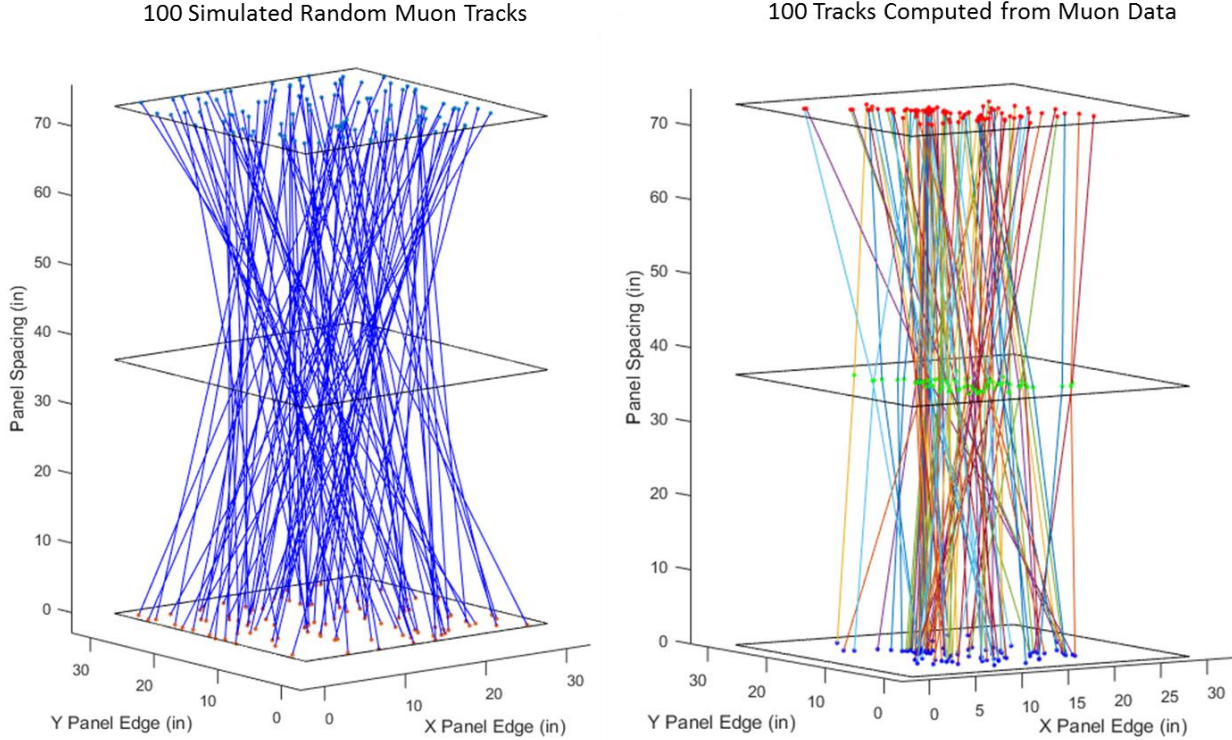


**Figure 29: Simulated random muon tracks (Left) and muon tracks computed from real data (Right). The model generated from the calibration dataset from the center panel was applied to all three scintillator panels.**

The majority of the computed muon tracks strike near the center of the panels rather than a random distribution as was expected. This observation can be attributed to several possible causes. First, the same model parameters were applied to all three panels rather than using individual models generated from the calibration data of each panel. Second, non-uniformities in the reflective coatings, the internal reflections of the panel, and in the couplings of each PMT could cause unnecessary complexity in the model fit from calibration data, introducing error in interpolation and repeatability. Third, the hole grid for LED calibration does not extend to the edges of the panel (24" square grid centered on a 30" square panel) which may make extrapolation beyond the grid unreliable. Finally, while the recorded signals are visually similar to those of muons, the application of light pulses from an LED placed on the surface of the panel may not accurately represent the interaction of a muon that struck at the same location. All of these possibilities are subjects of future work for this detector system.

## 4.4. Discussion

Stacked plastic scintillator panels with side mounted PMTs are an attractive technology to muon tracking experimentalists due to their modularity and ease of use. The potential for a low number of PMTs and simple configurability could lead to low-cost systems with many features, which could also make muon tracking accessible to a wider base of researchers and laboratories. The system described here has 3 panels but could easily be modified to have more than 10 panels. Each additional panel improves the precision of the computed track by making a best fit straight line to the data. As an example feature, in a many-panel system, an object could be placed between panel stacks and the angle of muon deflection from one stack to the next could be used to image the object. The frame of the present detector was designed to be robust, with outdoor applications and field deployments in mind but panels could be made smaller and less bulky frames can be constructed; trading some muon flux for potentially improved resolution and system maneuverability.

The LED calibration experiments provide insight into the implementation of gamma camera or “Anger logic” on large sheets of plastic scintillator with widely spaced PMTs mounted at the corners. Where PMTs with low transit time jitter could theoretically be used to directly triangulate muon interaction points in the present system, direct computation by magnitude is more complex. The traditional gamma camera approach computes a weighted sum (or difference) of response energies of a PMT grid attached to a scintillator crystal. The system is calibrated by placing a collimated gamma source in known locations and adjusting the weighting coefficients until the computed position matches the known position. This technique is effective with a closely spaced grid placed a significant distance from the edge of the scintillator. With the system described herein, having PMTs mounted on the corners of a large slab of plastic scintillator, assumptions of the traditional approach are no longer valid.

The theoretical relationship of measured intensity as a function of distance from the PMT is that of an exponential decay. While this relationship is supported by experimental data from LED flashes over the majority of the panel, the data shows deviation near the edges as well as significant local maxima in some locations beyond half way across the panel. This observation suggests that internal reflections and edge effects in the PVT slab are significant in the characterization of the optical intensity response over the full panel. This complex behavior suggests that machine learning from a calibration dataset may be an appropriate approach to implementing Anger logic on systems like the one described. The data discussed in this paragraph used a panel with no reflective coating.

Additional complexities are introduced by the practical difficulty of applying a uniform reflective coating to the faces of the PVT panel in an effort to improve photon collection efficiency. The tendency of applied foil to crease, wrinkle and bow leads to important nonlinearities across the

panel. It was observed that PMT responses can be significantly altered by simply flattening a bowed section of the foil against the panel face. Non-uniform reflective coatings make the intensity versus distance relationship less predictable and could cause large errors in data interpolation. A more uniform construction may be to use rigid reflective materials or even an optical coating deposited directly to the surface of the PVT.

## 4.5. References

- Aguiar P., Casarejos E., Silva-Rodriguez J., Vilan J. A., Iglesias A., Geant4-GATE Simulation of a Large Plastic Scintillator for Muon Radiography, *IEEE Transactions on Nuclear Science*, **62**, 2015.
- Alvarez, Luis W., Jared A. Anderson, F. El Bedwei, James Burkhard, Ahmed Fakhry, Adib Grgis, Amr Goneid, Fikhry Hassan, Dennis Iverson, Gerald Lynch, Zenab Miligy, Ali Hilmy Moussa, Mohammed-Sharkawi, and Lauren Yazolino, *Search for Hidden Chambers in the Pyramids*, *Science* **167**, 832-839, 1970.
- Anger H. O., Scintillation Camera, *Rev. Sci. Instrum.*, **29**, 27, 1958.
- Borozdin K.N., G.E. Hogan, C. Morris, W.C. Priedhorsky, A. Saunders, L.J. Schultz, and M.E. Teasdale, Surveillance: Radiographic imaging with cosmic-ray muons, *Nature* **422**, 277, 2003, doi: 10.1038/422277a.
- Borozdin, K.N COSMIC-RAY MUON TOMOGRAPHY AND ITS APPLICATION TO THE DETECTION OF HIGH-Z MATERIALS, 2005.
- Clarkson A., Hamilton D. J., Hoek M., Ireland D. G., Johnstone J. R., Kaiser R., Keri T., Lumsden S., Mahon D. F., McKinnon B., Murray M., Nutbeam-Tuffs S., Shearer C., Staines C., Yang G., Zimmerman C., The design and performance of a scintillation-fibre tracker for the cosmic-ray muon tomography of legacy nuclear waste containers, *Nucl. Instrum. Methods Phys. Res. A* , **745**, 138-149, 2014.
- George E. P., Cosmic rays measure overburden of tunnel, *Common- Wealth Engineer*, pp. 455–457, Jul. 1, 1955
- Gibert D., Beauducel F., Declais Y., Lesparre N., Marteau J., Nicollin F., Tarantola A., Muon tomography: Plans for observations in the Lesser Antilles, *Earth Planets Space*, **62**, 153-165, 2010.
- Lesparre N., Marteau J., Declais Y., Gibert D., Carlus B., Nicollin F., Kergosien B., Design and operation of a field telescope for cosmic ray geophysical tomography, *Geoscientific Instrumentation Methods and Data Systems*, **1**, 33-42, 2012.
- Marteau J., Bremond d'Ars J., Gibert D., Jourde K., Guardien S., Girerd C., Lanigro J. C., Implementation of sub-nanosecond time-to-digital convertor in field-programmable gate array: applications to time-of-flight analysis in muon radiography, *Measurement Science and Technology*, **25**, 2014.
- Nagamine, K., M. Iwasaki, K. Shimomura, and K. Ishida, Method of probing inner structure of geophysical substance with the horizontal cosmic ray muons and possible application to volcanic eruption prediction, *Nucl. Instrum. Meth.* **A356**, 585-595, 1995, doi: 10.1016/1068-9002(94)01169-9.

Pesente S., Vanini S., Benettoni M., Bonomi G., Calvini P., Checchia P., Conti E., Gonella F., Nebbia G., Squarcia S., Viesti G., Zenoni A., Zumerle G., First results on material identification and imaging with a large-volume muon tomography prototype, *Nuclear Instruments and Methods in Physics Research A*, **604**, 738-746, 2009.

Riggi S., La Rocca P., Leonora E., Lo Presti D., Pappalardo G. S., Riggi F., Russo G. V., Geant4 simulation of plastic scintillator strips with embedded optical fibers for a prototype of tomographic system, *Nuclear Instruments and Methods in Physics Research A*, **624**, 583, 2010.

Schultz L., Borozdin K., Gomes J., Hogan G., McGill, J., Morris C., Priedhorsky W., Saunders A., Teasdale M., Image reconstruction and material Z discrimination via cosmic ray muon radiography, *Nuclear Inst. and Methods*, **519**, 687-694, 2004.

Taira H., Tanaka H., A potential space- and power-effective muon sensor module for imaging a volcano, *Earth Planets Space*, **62**, 179-186, 2010.

Tanaka H., Uchida T., Tanaka M., Shinohara H., Taira H., Development of a portable assembly-type cosmic-ray muon module for measuring the density structure of a column of magma, *Earth Planets Space*, **62**, 119-129, 2010.

Uchida T., Tanaka H., Tanaka M., Development of a muon radiographic imaging electronic board system for a stable solar power operation, *Earth Planets Space*, **62**, 167-172, 2010.

## 5. CONCLUSIONS

Muons are subatomic particles that are more sensitive to density variation than other phenomena and can penetrate the earth's crust several kilometers. Their absorption rate depends on the density of the materials through which they pass. Currently, muon tomography can resolve features to the sub-meter scale. However, their practical use is uncertain because dependencies among resolution, duration of acquisition, density contrast, size of the target, and distance between target and detector remain undefined. To widen the performance envelope of muon technology, some of these parameters were addressed herein through a combination of modeling and experimental verification.

Results from this project lay the groundwork for future directions in this field. Low-density objects can be detected by muons even when enclosed in high-density material like lead and even small changes in density (e.g. changes due to fracturing of material) can be detected. Rock density has a linear relationship with muon scattering density per rock volume when this ratio is greater than 0.10. Limitations on using muon scattering to assess density changes among common rock types have been identified. However, other analysis methods may show improved results for these relatively low density materials. Simulations show that muons can be used to image void space (e.g. tunnels) within rock but experimental results have been ambiguous. Improvements are suggested to improve imaging voids such as tunnels through rocks. Finally, a muon detector has been designed and tested to measure muon direction, which will improve signal to noise ratio and help address fundamental questions about the source of upgoing muons.

#### 4. REFERENCES

- Alvarez, Luis W., Jared A. Anderson, F. El Bedwei, James Burkhard, Ahmed Fakhry, Adib Girgis, Amr Goneid, Fikhry Hassan, Dennis Iverson, Gerald Lynch, Zenab Miligy, Ali Hilmy Moussa, Mohammed-Sharkawi, and Lauren Yazolino, *Search for Hidden Chambers in the Pyramids*, *Science* **167**, 832-839, 1970
- Borozdin, K.N., G.E. Hogan, C. Morris, W.C. Priedhorsky, A. Saunders, L.J. Schultz, and M.E. Teasdale, Surveillance: Radiographic imaging with cosmic-ray muons, *Nature* **422**, 277, 2003, doi: 10.1038/422277a
- Jourde, K, D. Gibert, J. Marteau, J. de Bremond d'Ars, S. Gardien, C. Girerd, J.-C. Ianigro, and D. Carbone, Experimental detection of upward going cosmic particles and consequences for correction of density radiography of volcanoes, *GEOPHYSICAL RESEARCH LETTERS*, VOL. 40, 6334–6339, 2013, doi:10.1002/2013GL058357
- Lesparre, N., D. Gilbert, J. Marteau, Y. Declais, D. Carbone, and E. Galichet, Geophysical muon imaging: feasibility and limits, *Geophysical Journal International*, 183, (3), 1348-1361, 2010, DOI:10.1111/j.1365-246X.2010.04790.x
- Nagamine, K., M. Iwasaki, K. Shimomura, and K. Ishida, Method of probing inner structure of geophysical substance with the horizontal cosmic ray muons and possible application to volcanic eruption prediction, *Nucl. Instrum. Meth.* **A356**, 585-595, 1995, doi: 10.1016/1068-9002(94)01169-9.
- Malmqvist, L., G. Jonsson, K. Kristiansson, and L. Jacobsson, Theoretical studies of in-situ rock density determinations using underground cosmic-ray muon intensity measurements with applications in mining geophysics, *Geophysics*, v. 44, no. 9, p. 1549-1569, 1979
- Mei, D. M., and A. Hime, Muon-induced background study for underground laboratories, *Physical Review D* 73 (5):053004, 2006
- Tanaka, H., K. Nagamine, N. Kawamura, S. N. Nakamura, K. Ishida, K. Shimomura, Development of a two-fold segmented detection system for near horizontally cosmic-ray muons to probe the internal structure of a volcano, *Nuclear Instruments and Methods in Physics Research A* v. 507, 657–669, 2003

## APPENDIX A: SANDIA MUON DETECTOR FRAME STRUCTURAL ANALYSIS

The structural analysis of the Muon detector frame is described in this document. Per 02/01/2016 conversation with McMaster Rep. Haley, yield strength of the 6061 aluminum shaft is 35,000 [psi]. Also note that the Von Mises failure criterion was adopted for all subsequent Solidworks simulations.

The structural analysis shows that the safety factors built in by design and materials are sufficient to provide a high level of confidence that the risk of load failure is inconsequential. The displacements shown in these images are exaggerated for demonstration purposes. The color key should be examined for numerical analysis. The loads applied throughout these simulations are extreme scenarios far beyond the loads that will be experienced in reality. Comparison of the stress on each component to the strength of the component is performed for suitability and safety factor determination. For example, the rotational axis shaft below could support approximately a 3000lb load before yielding where the actual load will be near 325lb.

### Rotational Axis Shaft

Each 6061 aluminum shaft is expected to shoulder half the weight of the upper muon frame, or approximately 325 [lb]. A Solidworks simulation with a Von Mises failure criterion was performed by applying a bearing load to the end of the shaft over the area where the flanged collar grips the shaft. The bearing was treated as an elastic fixture with a normal to surface spring rate of 29,000 [ksi]. At a total weight of approximately 6,000 [lb.], both shafts are expected to be at or near yield.

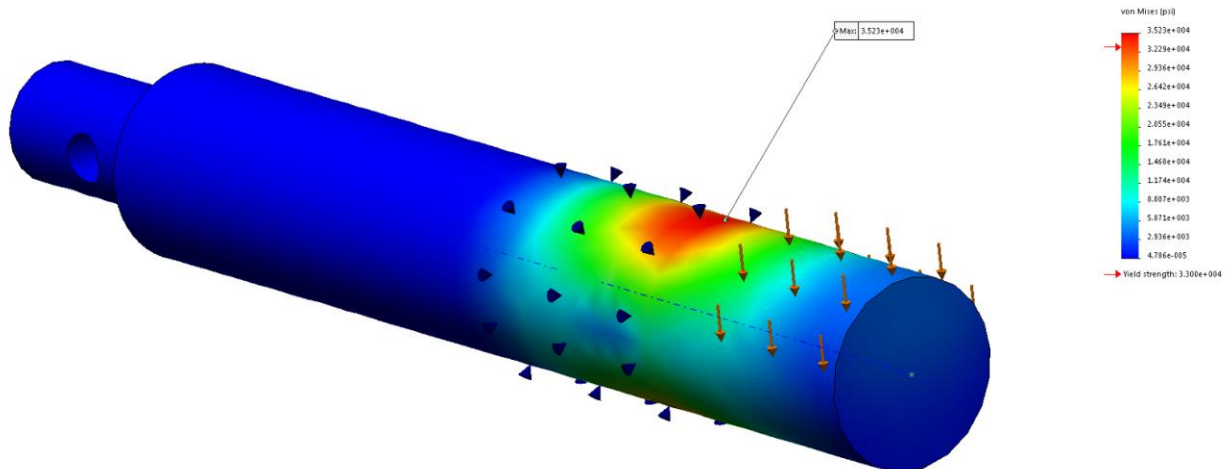


**Figure 30: Solidworks simulation of shaft with 3,000 [lbf] of sinusoidally distributed bearing load across collar cross section and elastically supported by bearing.**

If a factor of safety of 1.5 is applied to the analysis, the maximum usable weight of the structure is 4,000 [lb.]. The actual expected weight is thus 16.25% of the maximum usable weight.

## Flanged Collar Bolts

The initial design called for (3)  $\frac{1}{4}$ "-20,  $\frac{7}{8}$ " long 316 stainless steel socket head cap screws with yield strength of approximately 20 [ksi] to fasten the shaft collar to the indexing plate. As Figure 2 shows below, yield is approached at approximately 600 [lbf] loaded against one collar, or 1200 [lbf] of total upper frame loading.

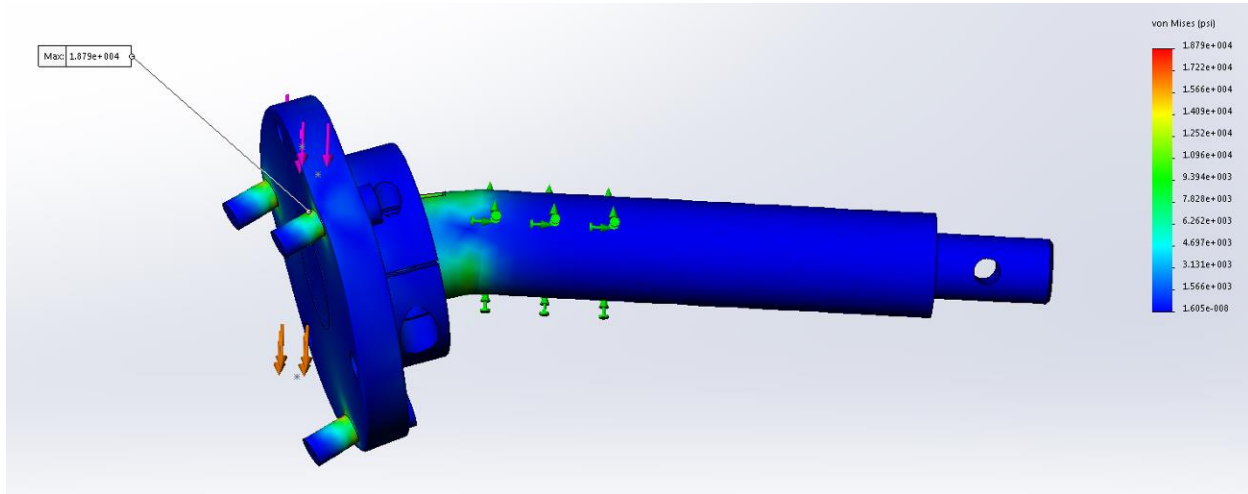


**Figure 31: Solidworks simulation at 600 [lbf] total loading across (3)  $\frac{1}{4}$ "-20 screws fastening the shaft collar to the indexing plate.**

This condition, which represents an anticipated loading that is 54% of the yield load, is intensified as the screws are preloaded to secure the collar to the indexing plate. To ameliorate the situation, the remaining (3)  $\frac{1}{4}$ " holes will accommodate (3) more  $\frac{1}{4}$ "-20 screws. Additionally, the stainless steel screws are to be replaced by grade 8 socket cap screws. The Solidworks simulation for this scenario is shown in Figure 3.

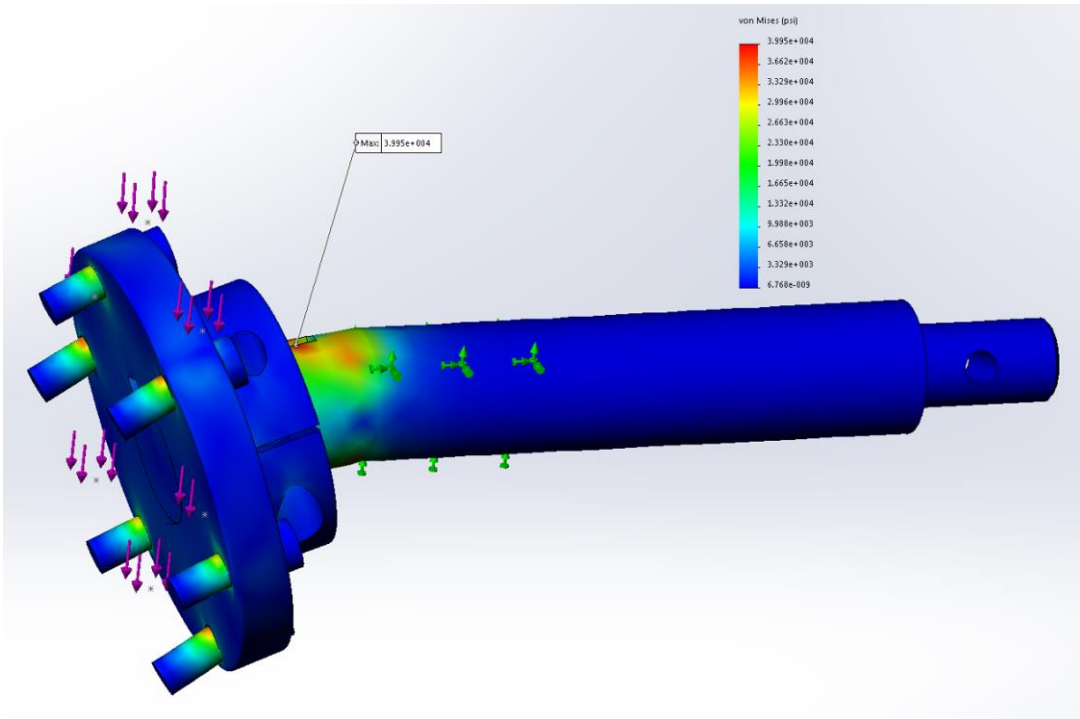


**Figure 32: Solidworks simulation at 2100 [lbf] total loading across (6) grade 8,  $\frac{1}{4}$ "-20 cap screws and zero frame stiffness.**

This simulation in Figure 3 represents a total loading scenario of 4,200 [lbf] including the weight of the upper frame. At such a loading, the maximum stress predicted by the simulation in any of the fasteners is approximately 35,000 [psi], compared to the average proof strength in grade 8 fasteners of 120,000 [psi]. The simulation neglects the stiffening effect of the frame and thus represents one extreme of the particular loading in which tension is introduced through deflection of the collar or bolts. Such a scenario is less taxing on the bolt's shaft but likely introduces tension on the bolt heads. It also introduces the possibility of bolt pullout from the indexing plate. Pullout from each plate may be expected at just shy of 1,500 [lbf] of lateral load, but there is virtually no possibility of such loading based on the structure's intended usage. The other extreme assumes a frame with infinite lateral stiffness such that the load produces nearly pure shear in the fasteners. As shown in Figure 4, loading at 4,200 [lbf] produces a maximum stress of roughly 37,000 [psi].

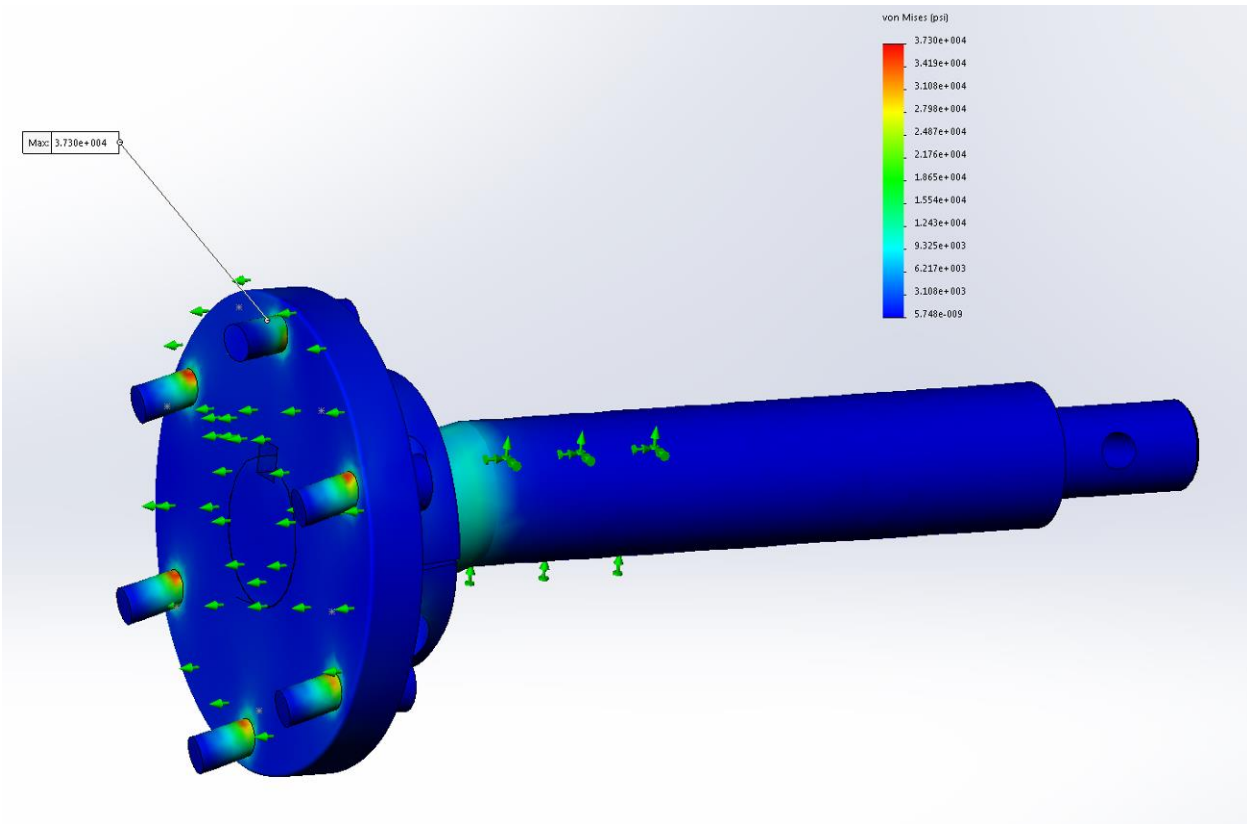


**Figure 33: Solidworks simulation at 2100 [lbf] total loading across (6) grade 8, 1/4"-20 cap screws and infinite frame stiffness.**

Finally, there is the possibility of bearing failure in the flange collar. Assuming a uniform load distribution across each bolt hole for simplicity, a total loading of 4,200 [lbf] would induce a stress of approximately 3,500 [psi] across each bolt hole in the collar, well below the collar's yield strength of XX [psi]. While bearing failure is not expected at this loading, localized yielding along the threads is expected.

#### Side Loading

With the base frame fixed from translating along the floor on its caster, loading in the direction parallel and perpendicular to the shafts is possible. The parallel loading case represents the limiting case due to the orientation of the column supporting the bearing; that is, the depth of the column in the parallel direction is 1.5" as opposed to 3.0" in the perpendicular direction. From figure 5, it can be seen that yielding is expected at approximately 400 [lbf] of lateral loading in addition to a slightly exaggerated upper frame loading of 650 [lbf] acting vertically on the columns through the bearing. Additional brace plates and brackets were later added to bolster the bending strength of the column/beam.

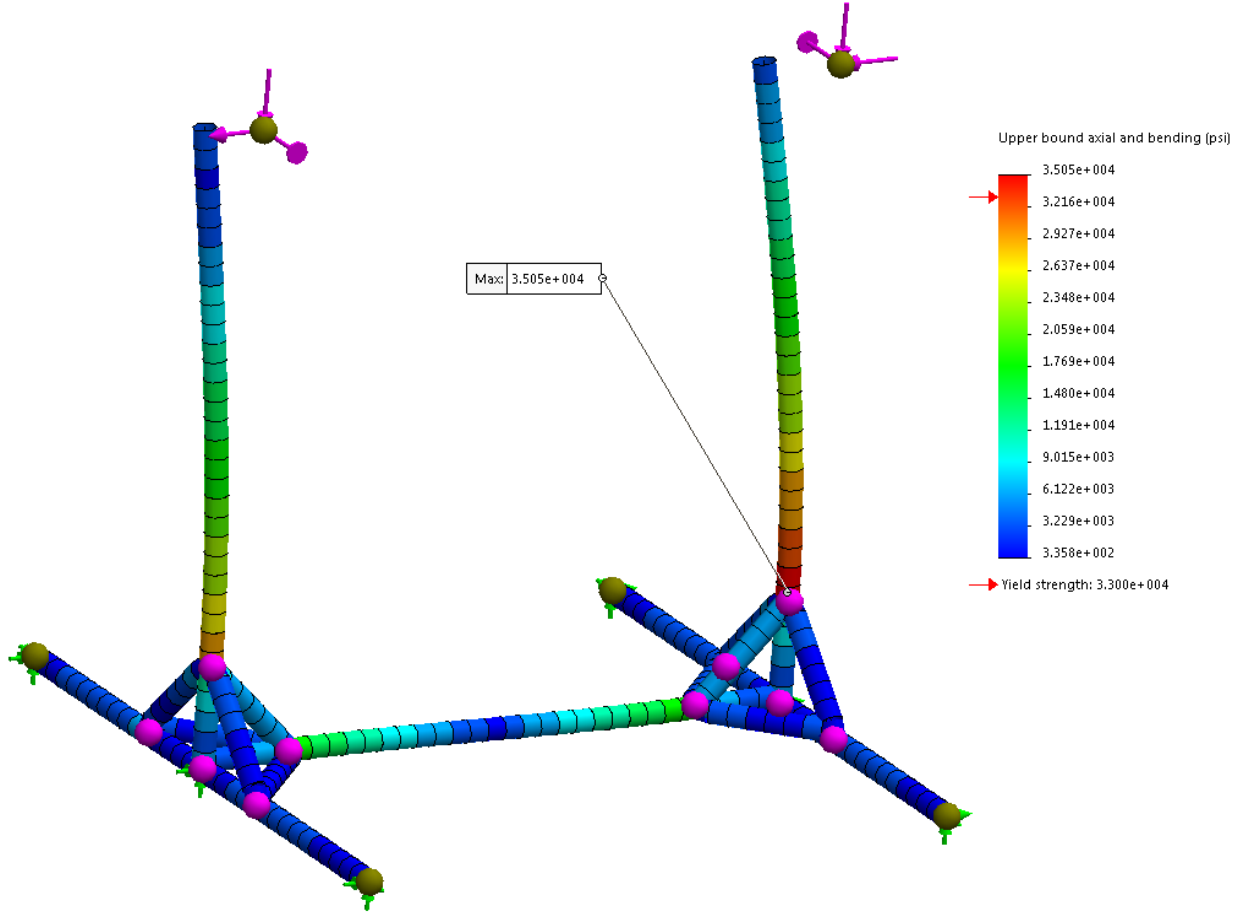


**Figure 34: Solidworks simulation at 400 [lbf] lateral loading and 650 [lbf] vertical loading on columns.**

#### Tip-Over Conditions

The structure is most susceptible to tipping when the normal to the scintillator plates is orientated at  $45^\circ$  to the ground, as shown in Figure 6, as this orientation maximizes the horizontal distance from the anticipated fulcrum (the locked outside casters).

In the least advantageous position, the midpoint of the caster wheels is 2.6" (measured along X) from the edge of the base support and 27.4" from the center of the bearing column. Tip over is expected when the moment of a force in the indicated position about the caster midpoint exceeds the moment of the upper frame's weight about the same point. The point of application of force  $L_{tip}$  is 24.6" from the caster midpoint.

$$L_{tip}(24.6 [\text{in.}]) = (650 [\text{lbf}])(27.4 [\text{in.}]) \rightarrow L_{tip} = 724 [\text{lbf}]$$

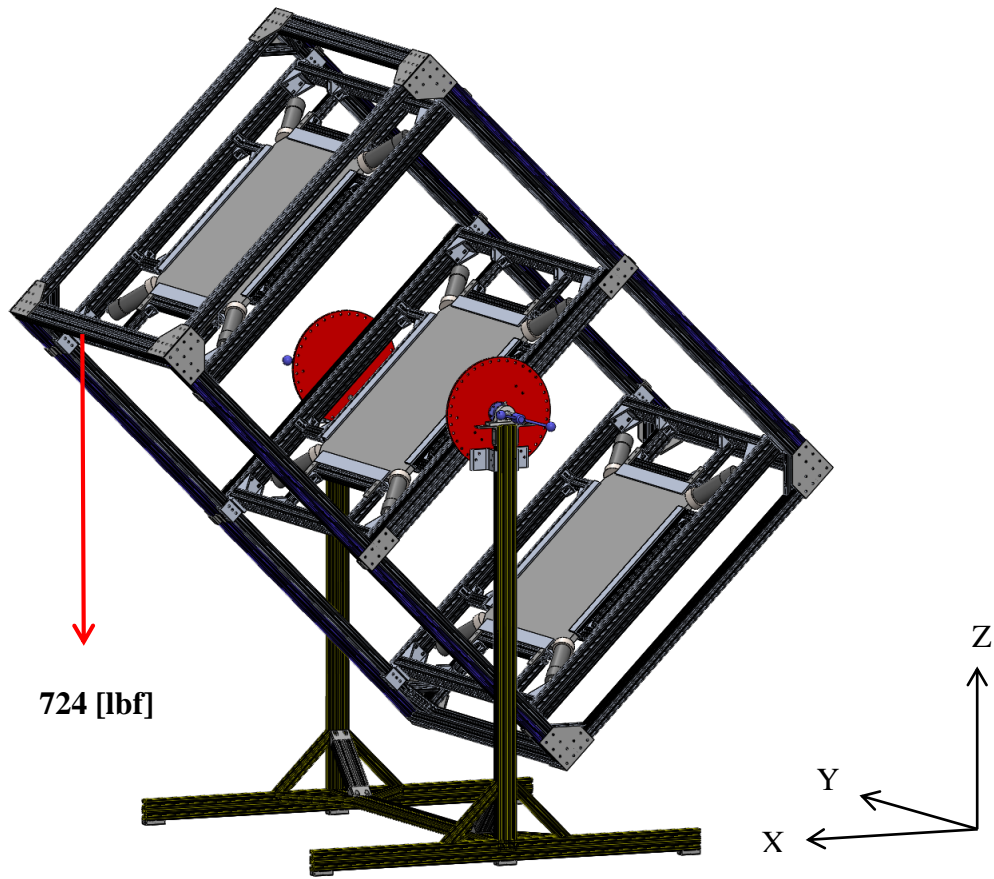


**Figure 35: Tip-over load of upper frame oriented at 45°.**

#### Horizontal Orientation Deflection

When the normal to the scintillator plates is parallel to the ground, some deflection at the ends of the 85" uprights is expected. Figure 7 shows an initial simulation run with 150 [lbf] applied at the four nodes at each of the ends of the structure for a total force of 1200 [lbf]. The extrusions in the simulation are 1.5x1.5". The anticipated maximum deflection was approximately 0.3".

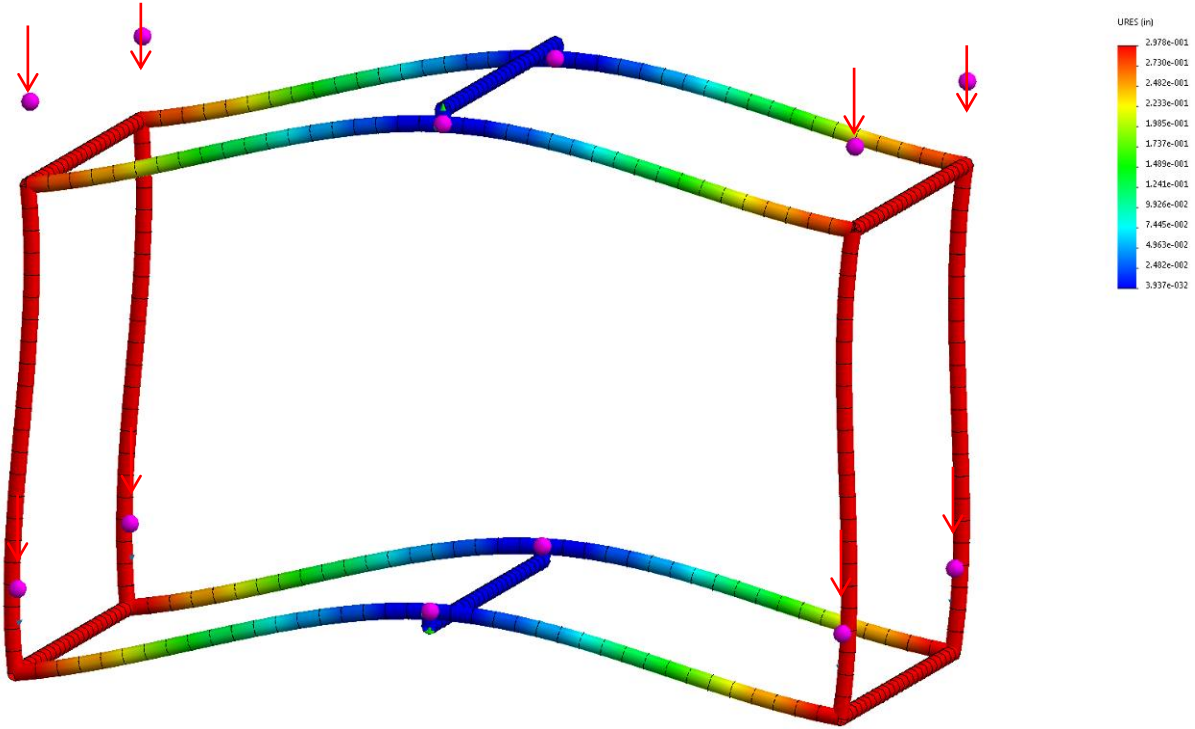


**Figure 36: Solidworks simulation for 1.5x1.5" extrusion frame in a horizontal orientation with 1200 [lbf] of loading applied at outlying nodes.**

The structure was eventually redesigned so that the 1.5x1.5" extrusions were replaced with 1.5x3.0" extrusions in an orientation preferable to bending (or the longest cross sectional dimension parallel to the loading). At twice the depth in bending, the expected deflection is 8 times less than original, or roughly 0.04". Obviously, the actual loading will be both less in total magnitude than simulated and distributed across the frame rather than applied locally at the outlying nodes. Thus, the above situation represents a fairly extreme case not likely to be observed while in operation.

#### Loading on the Rotational Cart

The column/beams that support the rotational assembly, under normal operating conditions, will experience two types of loading, both acting through the bearing: a vertical force corresponding to the upper frame weight and a moment due to the eccentric connection between the bearing and upper frame. The moment arm for each column/beam is approximately 2.7". Figure 8 shows a simulation for a total vertical load of 2000 [lbf] spread between the two column/beams.

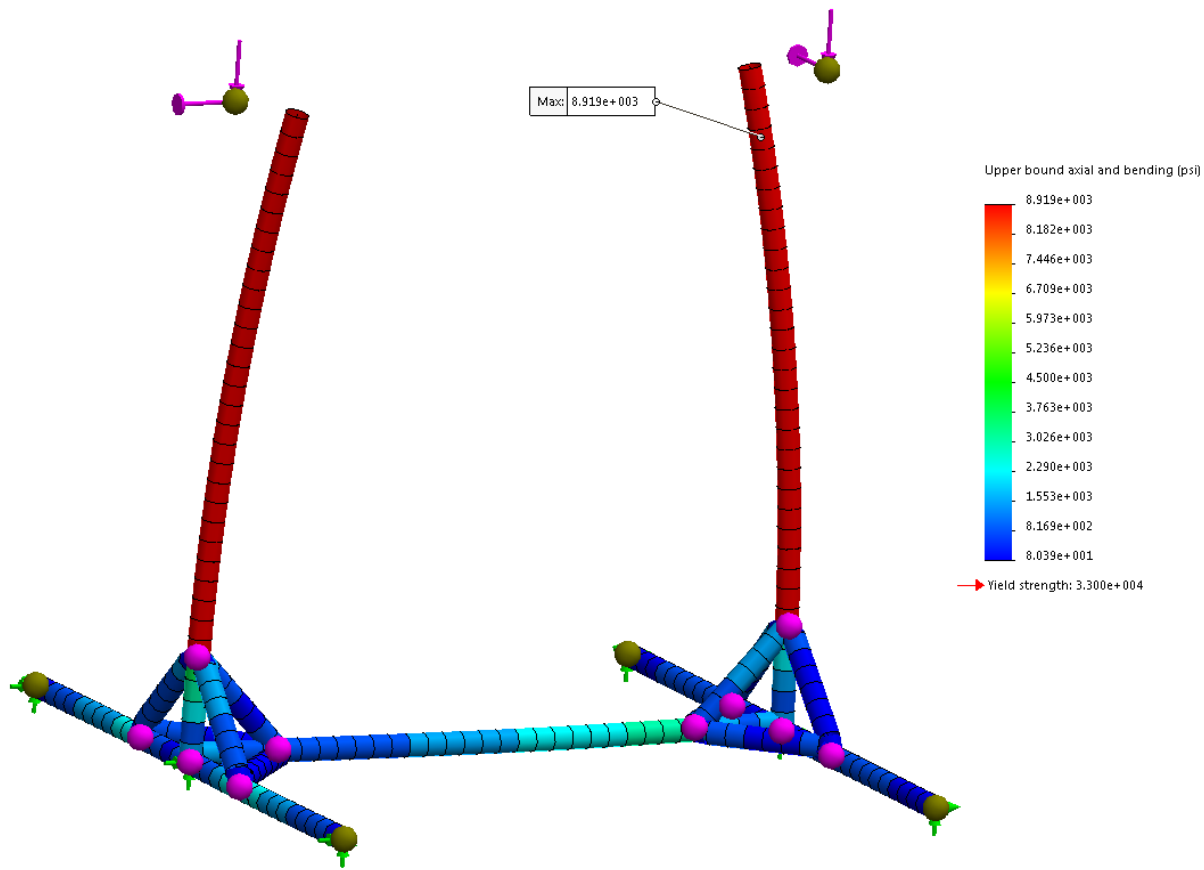


**Figure 37: Solidworks simulation of 2000 [lbf] combined vertical force and inward rotating moment of 2700 [lbf-in] acting on each column beam.**

As can be seen, the maximum bending stress in the column/beam is approximately a quarter of the yield strength of the extrusion and over 3 times the expected loading conditions on the rotational cart.

## **DISTRIBUTION**

1	MS0359	D. Chavez, LDRD Office	1911
1	MS0557	Nedra Bonal	1529
1	MS0750	Steve Vigil	6911 (electronic copy)
1	MS1033	Avery Cashion	6916 (electronic copy)
1	MS0899	Technical Library	9536 (electronic copy)



